2D Materials

PURPOSE-LED PUBLISHING™

TOPICAL REVIEW • OPEN ACCESS

Navigating growth regimes in graphene-assisted III-nitride epitaxy: insights, challenges, and pathways forward

To cite this article: Dominykas Augulis *et al* 2026 *2D Mater.* **13** 032005

View the article online for updates and enhancements.

You may also like

- Effect of pressure on the magnetic properties of $(Co_{0.5}Fe_{0.5})_5GeTe_2$
Tamás Prok, Zoltán Kovács-Krausz, Harvey Stanfield et al.

- Strain-enhanced altermagnetic spin splitting and ferroelectric polarization in multiferroic Cr_2X_2O (X = S, Se) monolayers
Yuxin Yang, Mengxu Lu, Qian Hu et al.

- Mesoscopic interferences in transport through $Ti_3C_2T_x$ MXene flakes
Oriane de Leuze, Sofiane Arib, Pauline de Crombrugghe et al.

This content was downloaded from IP address 158.129.162.202 on 04/11/2026 at 14:30

2D Materials

Check for updates

TOPICAL REVIEW

Navigating growth regimes in graphene-assisted III-nitride epitaxy: insights, challenges, and pathways forward

Dominykas Augulis*, Jūras Mickevičius, Arūnas Kadys and Tadas Malinauskas

Institute of Photonics and Nanotechnology, Faculty of Physics, Vilnius University, Saulėtekio al. 3, LT-10257 Vilnius, Lithuania

* Author to whom any correspondence should be addressed.

E-mail: dominykas.augulis@ff.vu.lt

Keywords: III-nitrides, graphene, growth regimes, epitaxial lift-off

OPEN ACCESS

RECEIVED
18 February 2026

REVISED
26 June 2026

ACCEPTED FOR PUBLICATION
2 August 2026

PUBLISHED
13 August 2026

Original content from this work may be used under the terms of the Creative Commons Attribution 4.0 licence.

Any further distribution of this work must maintain attribution to the author(s) and the title of the work, journal citation and DOI.

Abstract

The technological impact of III-nitrides in lighting and power electronics is well established. However, heteroepitaxy on rigid foreign substrates often results in high defect densities and limited mechanical compliance. This poses hurdles for the exploitation of electronic and photonic integrated circuits. Graphene interlayers offer an appealing alternative: by weakening interfacial adhesion while maintaining crystalline alignment under specific epitaxy conditions, they facilitate the lift-off of freestanding nitride membranes, allowing for substrate reuse. This review maps the experimental landscape with the theoretical background of graphene-assisted III-nitride growth, connecting macroscopic outcomes to competing interfacial regimes of van der Waals (vdW) epitaxy, quasi-vdW epitaxy, thru-hole growth, and remote epitaxy. Each process has a specific operational window under metal-organic chemical vapor deposition (MOCVD) conditions. Central challenges associated with the selection of a regime are traced to the exact root causes: suppressed nucleation on pristine graphene, uncontrolled defect formation and contamination during graphene preparation, and graphene degradation or interfacial reactions under the aggressive MOCVD environment, each of which can shift the dominant regime. Recent advances in direct graphene synthesis, controlled functionalization, buffers, and flow-modulation schemes have been assessed as practical routes to coalesced, transferable GaN- and AlN-based membranes, which constitute the main focus of this review. Future priorities for field advancement include standardized metrics for distinguishing growth modes, robust interface engineering, and considerations for novel device creation.

1. Introduction

Over the past few decades, III-nitride semiconductors have emerged as the cornerstone of modern photonic and electronic devices, owing to their remarkable electrical, optical, and thermal properties. The direct bandgap, tunable across the range from 0.7 to 6.2 eV, enables applications in light-emitting diodes (LEDs) and laser diodes covering visible and ultraviolet (VIS/UV) wavelengths [1–3]. The high electron mobility and high breakdown field of III-nitrides make the material ideal for high-power and high-frequency electronics [4–6]. Fascinatingly, nitride-based devices have become commercialized, relying completely on heteroepitaxial approaches. Despite some progress, bulk III-nitride substrates remain largely unavailable for industrial use due to the difficulties in growing large-scale and high-quality crystals [7–9]. As a result, foreign substrates such as sapphire, SiC, and silicon are widely used [10, 11]. However, significant lattice and thermal expansion mismatches between III-nitrides and these substrates often introduce high defect densities, which can degrade device performance. To address these challenges, various advanced epitaxial growth techniques have been developed to reduce defects and improve material quality.

For next-generation semiconductor applications, technologies enabling multi-functionality, heterogeneous integration, and flexible form factors are becoming increasingly important [12–19]. Traditional solid-state thin film templates, however,

© 2026 The Author(s). Published by IOP Publishing Ltd

are typically brittle and rigid, limiting their use in such applications. Consequently, freestanding GaN membranes are highly desirable. Common methods for releasing nitride thin films from rigid substrates, such as chemical etching of the Si substrate or laser lift-off from the sapphire substrate, can cause increased surface roughness and material damage [15, 18, 20, 21].

Two-dimensional (2D)-material-assisted epitaxy has recently emerged as a promising route to high-quality freestanding GaN membranes [13, 16–19, 22, 23]. In this approach, 2D materials such as graphene or hexagonal boron nitride (h-BN) are pre-deposited on the substrate before epilayer growth. These layered materials, bound together by van der Waals (vdW) forces, weaken the bonding at the interface, yet still permit epitaxial alignment during growth. At the same time, the reduced adhesion enables the film to be mechanically exfoliated from the template.

The presence of a 2D interlayer creates a distinct interface where different growth regimes may develop, depending on atomic-level bonding and nucleation. Among these, ***vdW epitaxy*** refers to growth on a 2D material surface where bonding occurs exclusively through weak vdW forces, without any interaction with the underlying substrate [12, 13, 18, 19, 22, 24, 25]. This mechanism is independent of the substrate underneath and can occur even when the 2D material is freestanding. Since the interface between the epilayer and 2D layer is governed solely by vdW forces, vdW epitaxy provides the most straightforward route to reduce interfacial adhesion. In addition, the absence of strong chemical bonding greatly relaxes the lattice-matching constraints. However, the lack of dangling bonds on the surface of the 2D layer suppresses nucleation, which can lead to polycrystalline or poorly oriented growth [12, 18, 24].

To address the nucleation issue, defects can be intentionally introduced into the 2D layer, either through doping [23, 24, 26] or surface treatment [13, 18, 23], leading to a growth mode known as ***quasi-vdW (QvdW) epitaxy***. In this regime, growth proceeds through a hybrid mechanism: chemical bonding at defect sites combined with vdW interactions in other regions, established through lateral growth. A drawback of this approach is that the crystal quality of the epilayer becomes partially dependent on the quality of the 2D material itself [12, 19, 24]. A related regime, ***thru-hole epitaxy***, relies on nucleation at the substrate exposed via nano-holes in the 2D layer [17, 19]. While this allows the epilayer to inherit the substrate's crystal orientation, direct bonding at the exposed sites may hinder complete exfoliation [27].

Alternatively, when the 2D interlayer is sufficiently thin, typically one or two monolayers, the electrostatic potential of the underlying substrate can partially penetrate through the 2D layer and influence the crystallographic orientation of the growing epilayer, even without direct chemical bonding. This regime is known as ***remote epitaxy*** [12–14, 17–19, 24–26, 28].

The material quality of the freestanding membrane remains the most important factor in selecting the preferred growth mechanism. Interface adhesion is also crucial for achieving controllable exfoliation. Ultrathin 2D interlayers are critical for exfoliation; yet, they degrade under the high temperatures and reactive conditions typical of III-nitride growth [17, 23, 26]. As the 2D layer thickness increases, the electrostatic potential field of the substrate becomes more strongly screened [12, 13, 17–19, 24–26]. In practice, these competing limitations often blur the distinctions between growth regimes.

All of these growth regimes have been extensively discussed in the scientific literature. Recent review papers have focused primarily on comparing different growth regimes or on selected regimes in the context of applications [13, 14, 18, 19, 29–31]. Herein, we present a comprehensive overview of graphene-assisted epitaxy of III-nitride semiconductors, spanning the underlying adsorption mechanisms through the resulting material properties, with particular emphasis on processes specific to metal-organic chemical vapor deposition (MOCVD). The review focuses primarily on GaN- and AlN-based structures, reflecting the current literature, while InN is considered only where relevant to general adsorption trends. We begin by summarizing theoretical insights into adatom adsorption and migration on graphene and highlighting how surface energetics, chemical inertness, and electrostatic transparency establish the conditions for epitaxial growth. We then outline practical routes for graphene deposition and the key characterization methods used to assess graphene quality and interface integrity. The central part of the review focuses on early-stage III-nitride growth on graphene-based templates, emphasizing recurring challenges, including graphene degradation during nucleation and high-temperature coalescence, as well as unintended interfacial reactions. Membrane exfoliation techniques are then discussed, providing additional insights into the growth regimes and emphasizing their role in producing freestanding layers. Finally, we conclude with an outlook on future research directions, highlighting the need for robust graphene integration and advanced interfacial engineering.

2. Adsorption on graphene mechanisms

At the fundamental level, the initial stages of the epilayer growth are governed by adsorption. In this chapter, we review the adatom adsorption on graphene, focusing on their interactions with the graphene surface. The role of dangling bonds is analyzed in defective graphene, where localized states can

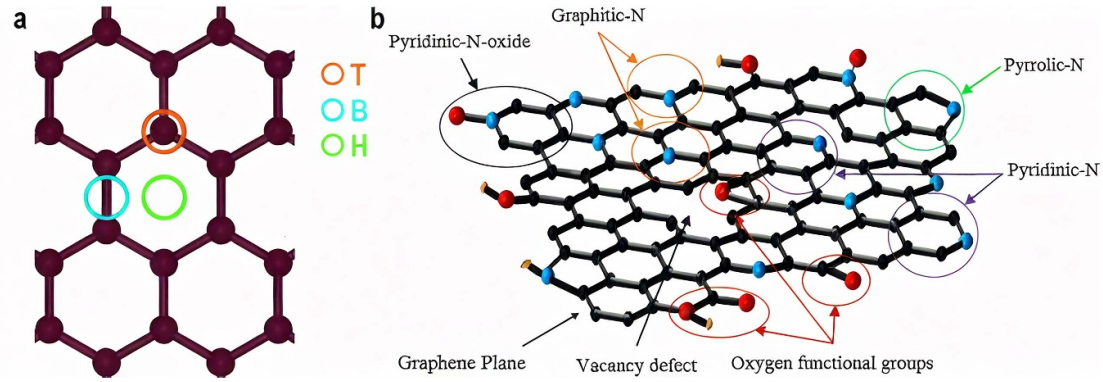

Figure 1. Graphene adsorption sites and representative defect configurations. (a) Schematic top view of the three high-symmetry adsorption positions on graphene: hollow site (H) at the center of a hexagonal ring, bridge site (B) above a C–C bond, and top site (T) above a carbon atom. (b) Examples of structural and chemical imperfections in graphene, including vacancy defects, graphitic-N, pyridinic-N, pyrrolic-N, pyridinic-N-oxide, and oxygen-containing functional groups. Atom colors in panel (b) denote carbon (black), nitrogen (blue), oxygen (red), and hydrogen (orange). Reprinted from [43], Copyright (2021), with permission from Elsevier. Resolution enhanced for clarity.

strongly modify the adsorption behavior and nucleation pathways compared with pristine surfaces. In contrast, lattice transparency is emphasized as the key mechanism enabling remote epitaxy, allowing the electrostatic potential to penetrate through the graphene layer and guide adatom adsorption.

2.1. Pristine graphene

The hexagonal arrangement of carbon atoms in the basal plane of graphene forms a highly stable, low-energy surface [32]. Due to the absence of reactive dangling bonds, adatoms primarily interact with the surface via vdW forces. First-principles calculations based on density functional theory (DFT) have been performed to study the interaction of adatoms with the graphene surface [33–42]. Three high-symmetry adsorption sites are typically considered: the hollow (H) site at the center of a hexagonal ring, the bridge (B) site at the midpoint of a carbon-carbon bond, and the top (T) site directly above a carbon atom (figure 1 (a)). Each site presents a distinct local electronic environment that affects both the binding strength and the surface mobility of incoming adatoms.

For group-III metals (Al, Ga, and In), the most energetically favorable adsorption site is near the H site [33–36, 38–40, 42]. Although the absolute values of adsorption energy vary depending on the calculation method, a consistent trend emerges: adsorption energy decreases with increasing atomic number [33, 34]. Ga adatoms show moderate binding affinity to the graphene surface, with adsorption energies ranging from −0.858 to −1.52 eV, depending on the computational method [33, 34, 39, 42]. While adsorption is primarily governed by vdW interactions, calculations of the electron localization function [42] and charge transfer analysis [33, 35, 36, 39, 40] reveal partial charge transfer into the delocalized electron system of graphene. Adsorption at the H site is further associated with a low diffusion barrier [34, 39, 42], with values as low as 0.03 eV reported for Ga adatoms [34], allowing them to remain mobile on the surface and promoting island formation.

Nitrogen adatoms preferentially adsorb at the B site, with calculated adsorption energies between −0.83 and −0.98 eV [37, 38, 40–42]. As the N adatom gains partial charge from graphene [40], adsorption locally disrupts the π-bonding network, leading to partial rehybridization and lattice distortion [37, 40], which is characteristic of covalent bonding. Recently, a more complex adsorption mechanism has been suggested, based on electron localization function calculations: at an initial distance of 3 Å, N adatoms interact only weakly with the graphene surface and slide from the H site toward the B site. During this transition, they must overcome an energy barrier before descending to form covalent bonds [42]. Stronger bonding leads to a high diffusion barrier of 0.86 eV [41, 42], indicating that N atoms can effectively initiate nucleation.

2.2. Defective graphene

Adatom adsorption is significantly enhanced at defect sites on the graphene surface. Lattice imperfections such as vacancies, dopant atoms, grain boundaries, and step edges increase the chemical reactivity of graphene by introducing dangling bonds and/or by creating preferential binding sites (figure 1(b)) [27, 41, 43–47].

For the simplest defect, a single vacancy, DFT calculations show that various atoms readily adsorb at the vacancy site, exhibiting markedly higher adsorption energies compared to pristine graphene [35, 41, 48–52]. Although foreign adatoms can also bind at sites adjacent to the vacancy, the vacancy itself remains the most energetically favorable location [41, 48, 50, 51]. The enhanced stability arises from the broken π-bonding network surrounding the vacancy,

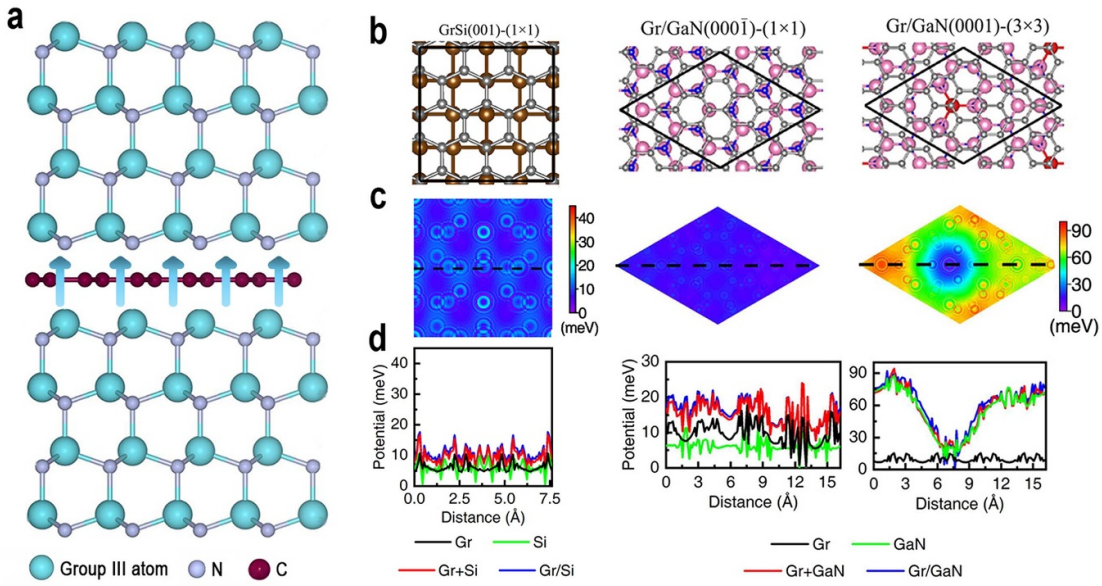

Figure 2. (a) The structural representation of a remote epitaxial wurtzite III-nitride layer with the (0001) orientation on a graphene/native template. (b) Top views of the graphene/Si(001)-(unreconstructed surface), graphene/GaN(000$\bar{1}$)-(unreconstructed surface) and graphene/GaN(000$\bar{1}$)-(extra Ga per 3 × 3 cell) interfaces. The brown, pink, blue, and gray balls represent Si, Ga, N, and C atoms, respectively. (c) Potential fluctuation maps of the three interfaces. (d) Potential fluctuations of the isolated graphene, Si, and GaN substrates, potential sum graphene+Si and graphene+GaN, and compound templates graphene/Si and graphene/GaN along the black dashed lines in (c). Reproduced from [40]. © IOP Publishing Ltd All rights reserved.

which introduces unpaired electrons [53, 54]. Among the studied species, N adatoms exhibit the highest adsorption energy [48–50]. Owing to the proximity of carbon and nitrogen in the periodic table, N adatoms are readily incorporated into the graphene lattice, forming strong covalent C–N bonds [41, 55] and yielding N-doped graphene.

The adsorption behavior on doped graphene surfaces strongly depends on the type of dopant and local configuration. Computational studies have primarily focused on nitrogen and oxygen impurities, whereas metal doping has received less attention [38, 48, 50, 52, 56]. DFT calculations indicate that substitutional oxygen impurities significantly reduce the stable adsorption of Ga and N adatoms [50]. The strong electronegativity and relatively large atomic size of oxygen prevent substitutional oxygen doping, whereas the attachment of oxygen groups, such as epoxyl and carbonyl, induces a transition from sp^2 to sp^3 hybridization [55]. These states exhibit strong binding affinities for Ga and N adatoms, providing favorable adsorption sites [47].

Nitrogen doping results in graphitic, pyridinic, or pyrrolic configurations, each with distinct bonding environments [43, 55, 57]. The graphitic configuration introduces extra electrons into the π-bonding system [43, 55], slightly decreasing the adsorption energy of Ga and N adatoms [50], and modestly enhancing the binding affinity of Al adatoms [52]. In contrast, pyridinic and pyrrolic nitrogen configurations, which are associated with carbon vacancies or edge sites, withdraw electrons from the π-bonding network [43]. This localized electron deficiency significantly increases the adsorption energy of the Al adatoms [38, 56], indicating stronger chemical interactions.

Structural imperfections in the graphene layer, such as steps, wrinkles, and folds, create kinked and ledged sites on the surface. These sites provide energetically favorable nucleation centers even without generating dangling bonds, as the associated local curvature forms potential wells and reduces adatom migration [45, 46].

2.3. Remote interaction with the substrate

Another factor that strongly affects adatom adsorption on the graphene surface is the substrate beneath the graphene layer. DFT calculations revealed that the adsorption energies of Ga and N adatoms increase when graphene is supported on sapphire or GaN substrates [39, 40]. This adsorption enhancement is attributed to two mechanisms: substrate-induced potential fluctuations that penetrate through the thin graphene layer and define the energetically favorable adsorption sites [39], and interface charge transfer (or redistribution) [40].

The ability of the substrate-generated electrostatic field to propagate through graphene and influence the adatom arrangement on its surface without direct chemical bonding is referred to as the lattice transparency (figure 2(a)) [39, 40, 58–60]. This behavior arises from the lack of both in-plane and out-of-plane bond dipole moments in the graphene lattice. The effectiveness of lattice transparency is governed by the

Table 1. Electrostatic potential fluctuations (in meV) at the graphene surface for different substrate terminations and reconstructions. Data adapted from Hou *et al* [40].

Substrate and surface type	Potential (meV)	Notes
Si(001)-(1×1)	19.25	Unreconstructed surface
Si(001)-(2×1)	39.85	Reconstructed with dimers
GaAs(001)-(1×1)	19.31	Unreconstructed surface
GaAs(001)-β(2×4)	88.72	Arsenic-stabilized reconstruction
GaN(000$\bar{1}$)-(1×1) N-terminated	25.96	Unreconstructed surface
GaN(000$\bar{1}$)-(1×1) Ga-terminated	28.05	Unreconstructed surface
GaN(000$\bar{1}$)-(3×3)	93.31	Ga adatoms present
GaN(0001) Ga-terminated	72.42	Distorted graphene interface

thickness of the graphene layer and polarity of the substrate [58, 60–64]. Substrates with a higher bonding ionicity, such as GaN, AlN, and sapphire, induce stronger electrostatic coupling across the graphene layer, allowing multiple graphene layers to be inserted without fully screening the potential field. In contrast, low-polarity substrates such as Si exhibit much weaker electrostatic modulation, and even a single graphene monolayer is sufficient to screen the field [58, 60, 61].

A detailed analysis of electrostatic potential fluctuations on graphene-covered Si, GaAs, and GaN templates shows a strong dependence on surface orientation, termination, and reconstruction (figures 2(b)–(d) and table 1) [40]. However, only a weak correlation between adatom adsorption and these potential fluctuations was found, indicating that the interface charge transfer (redistribution) plays a more dominant role. In this mechanism, the graphene layer not only allows the substrate-generated electrostatic field to propagate through it but also mediates it. When a localized negative charge from the underlying substrate approaches the bottom surface of the graphene layer, the downward-facing p_z orbitals of the carbon atoms become positively polarized due to the absence of direct electron sharing or bonding. To maintain charge neutrality, the upward-facing p_z orbitals acquire the corresponding negative polarization. Through this induced dipole-like mechanism, the p_z orbitals effectively mediate the transfer of the surface charge pattern of the underlying substrate to the top surface of graphene [39, 40, 65]. DFT calculations show that changing the surface orientation can modify the interface charge transfer and the magnitude of the adsorption energy, and may even reverse the relative adsorption preferences of cations and anions [40].

The concepts of lattice transparency and interface charge transfer have recently been combined under the framework of attenuated charge transfer [63]. Bader charge analysis of an N adatom adsorbed on graphene supported by a SiC substrate shows that the substrate charge is partially transferred through the graphene to the adatom, with the degree of charge transfer becoming increasingly attenuated as the number of graphene layers increases.

3. Graphene deposition

The dominant adsorption mechanism depends on the structural and electronic properties of the deposited graphene, highlighting the importance of selecting an appropriate deposition technique (figure 3). Conventional strategies for integrating graphene into the epitaxy of III-nitrides rely on either direct growth or polymer-assisted wet/dry transfer; yet both approaches introduce defects or degrade the graphene layer [17, 22, 26, 28, 66–76]. Alternative methods, such as electrochemical bubble transfer, enable polymer-free transfer and high surface cleanliness. However, they are inherently limited to highly conductive substrates, restricting their applicability for III-nitride growth on insulating platforms such as sapphire, SiC, or GaN. Similarly, non-electrochemical bubble transfer avoids polymer residues but typically suffers from slow processing and a high risk of mechanical deformation during delamination [66, 69, 71, 74, 76].

Recent progress in wafer-scale graphene synthesis and transfer has substantially improved the availability of large-area graphene templates. Emerging approaches, including ice-assisted transfer [77], switchable ferroelectric-polymer-assisted transfer [78], conformal-contact-assisted transfer [79], and UV-tunable adhesive tapes [80], have demonstrated cleaner large-area transfer with reduced mechanical damage and residue formation. Although these methods have not yet become standard in III-nitride 2D-material-assisted epitaxy, they represent promising routes for improving graphene continuity and interfacial cleanliness.

Nevertheless, the requirements for graphene as an epitaxial interlayer are significantly more stringent than those for applications such as transparent electrodes or electronic channels. Even small amounts of polymer residue, trapped water, wrinkles, cracks, pinholes, layer-number variation, or rotational disorder can modify the vdW gap, screen remote electrostatic coupling, introduce unintended nucleation sites, and locally shift the growth mode toward QvdW or thru-hole epitaxy [60, 64, 81]. As a result, while transferred graphene may be sufficient for proof-of-concept III-nitride epitaxy and exfoliation, it has not

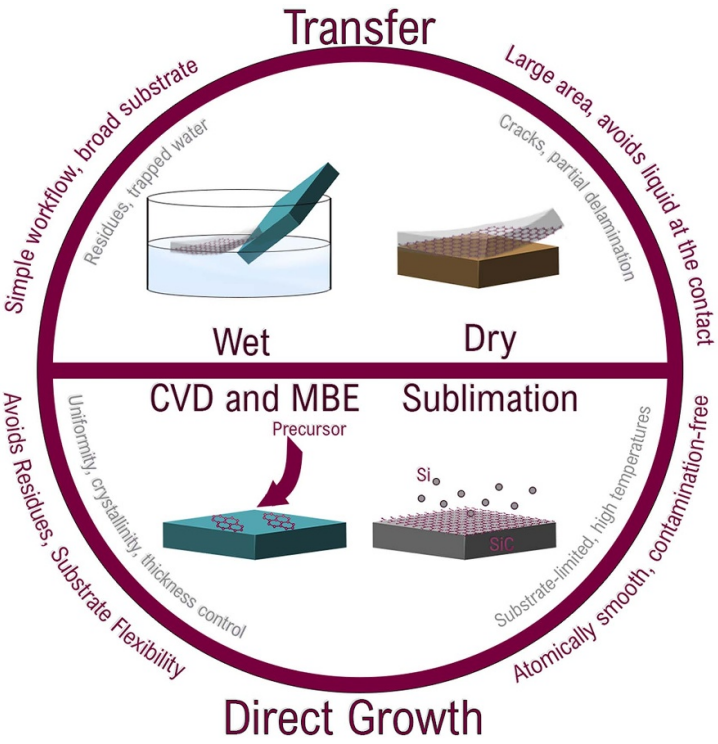

Figure 3. Schematic summary of the common graphene integration strategies used for 2D-material-assisted III-nitride epitaxy, grouped into transfer-based and transfer-free/direct growth routes. Key practical trade-offs are highlighted.

yet achieved the level of reproducibility required for industrial-scale templates. To address these limitations, we examine the transfer approaches and direct growth strategies in more detail.

3.1. Wet transfer

The traditional wet transfer method is the most widely used approach for depositing graphene onto epitaxial templates, owing to its simplicity, minimal equipment requirements, and widespread availability of commercially produced graphene films [82–101]. Graphene is typically synthesized on metal foils, such as copper or nickel, and coated with a polymer support layer to preserve structural integrity during handling. Standard wet transfer techniques use chemical etchants and solvent-assisted delamination to detach graphene from the growth substrate. After etching the metal, the graphene-polymer stack is released and floated on deionized water before being transferred onto the target substrate. Post-transfer cleaning, usually by solvent rinsing or thermal annealing, is then applied to remove residual contaminants and restore the surface cleanliness. Despite its practicality, wet transfer often introduces process-induced defects, including polymer residues, wrinkles, water entrapment, and mechanical tears [83, 84, 87–89, 91–93, 95–101], all of which can degrade surface quality and interfere with nitride epitaxy.

Poly(methyl methacrylate) (PMMA) is the most commonly used support layer because of its established processing method and compatibility with standard etching protocols [82–84, 86–89, 93, 94, 96, 99–101]. Alternative polymer scaffold materials have been studied for mitigating PMMA-related contamination [84, 86–88, 91, 95, 97, 98]. Notably, poly(bisphenol A carbonate) yields cleaner transfer by dissolving readily in chloroform at room temperature, removing the need for high-temperature annealing, thereby reducing surface roughness, doping effects, and residual contamination [87]. Other polymers, including poly(lactic acid), poly(phthalaldehyde), and paraffin, have shown promise in reducing transfer-induced contamination, but they have not been widely adopted due to limited mechanical stability and greater processing complexity [87, 95]. Consequently, PMMA remains the de facto standard for laboratory-scale applications owing to its procedural robustness and reproducibility despite its known shortcomings.

In addition to residues from the polymer supports, the metal etching step introduces impurities that can further compromise the quality of graphene. Common etchants such as ammonium persulfate ($(NH_4)_2S_2O_8$), ferric chloride ($FeCl_3$), and mixtures of hydrogen peroxide with hydrochloric acid (H_2O_2/HCl) often leave ionic species and reaction by-products that are difficult to remove [85, 86, 90, 93, 101]. These etchant residues, together with polymer remnants and water intercalation at the graphene-substrate interface, can promote delamination, bubble formation, and a loss of interfacial

conformity [92, 101]. Such contaminants modify the surface chemistry of graphene and compromise its effectiveness as an electrostatically transparent and structurally uniform interfacial layer.

3.2. Dry transfer

To address the inherent contamination and limited scalability of wet transfer, dry transfer techniques that minimize chemical exposure have been developed [82, 99, 100, 102–114], along with roll-to-roll transfer for large-area integration [115–118] and support-free methods that eliminate polymer residues [119, 120]. Dry techniques avoid liquid contact during the final placement of the graphene layer using mechanical delamination, often assisted by adhesives or thermal-release layers, followed by dry deposition onto the receiving substrate. Although a solvent may still be required to remove the intermediary adhesive or scaffold used for initial removal, the critical distinction is the absence of direct liquid exposure at the graphene-target interface, which reduces interfacial impurities and helps preserve an optimal vdW gap essential for remote epitaxy.

The graphene stack is delaminated from the growth substrate by exploiting the adhesion energy differences between the support and growth substrate. Typically, different polymer layers and/or thermal-release tape (TRT) are used as sacrificial supports and mechanical backing layers [82, 100, 102, 104, 106–108, 111–118]. Another method employs an inorganic metal-oxide lifting layer with a low interfacial binding energy [110]. Layer-resolved graphene transfer utilizes a metal decoupling layer deposited atop graphene, with TRT serving as a mechanical handle to peel graphene from its growth substrate [103, 105]. After transferring the graphene and its support onto the target substrate, the support is removed through thermal or UV exposure for mechanical detachment, or alternatively dissolved in mild solvents, yielding a relatively clean deposition [82, 99, 103, 105, 106, 108, 111, 112, 114–116].

Despite minimizing water insertion, dry transfer techniques still present notable limitations. Mechanical stresses arising during lamination and peeling can result in cracks, wrinkles, or partial delamination [100, 102, 111, 114, 116]. Furthermore, successful exfoliation from the growth substrate often requires pre-oxidizing the metal surface to weaken the interfacial bonding, which introduces additional complexity and potential variability in the process [106, 111, 112, 114]. Consistently achieving high-quality graphene transfer, therefore, demands precise control over both mechanical and chemical parameters.

3.3. Sublimation from SiC

Since transfer processes often introduce contamination or damage, they cannot reliably produce the clean, continuous interfaces and precise interfacial spacing required for certain 2D-material-assisted epitaxy regimes. To address these limitations, direct growth techniques have emerged as a promising route for achieving the material quality required for controlled epitaxial growth. In this section, we focus on graphene synthesized by thermal sublimation of SiC, while direct chemical vapor deposition (CVD) growth is discussed in the following section.

Graphene synthesis by SiC sublimation is performed by heating a SiC wafer to high temperature in a vacuum or an inert gas atmosphere. During thermal decomposition of SiC, Si–C bonds are broken, and silicon atoms are sublimated from the SiC substrate, while the remaining carbon atoms rearrange to form a graphene structure [121–123]. The graphitization process is strongly influenced by the polarity of the SiC surface [121, 123, 124]. On the Si-face (0001), the growth starts with the formation of a buffer layer, a carbon layer similar to graphene, but containing sp^3 atoms sharing covalent bonds with SiC [121, 122]. Above this buffer layer, uniform monolayer or bilayer graphene, also called epitaxial graphene (EG), can be grown with excellent thickness control [123]. In contrast, the C-face ($000\bar{1}$) decomposes more rapidly, often producing multilayer graphene with rotational stacking and less uniformity [121, 123]. For applications requiring precise interface control, such as remote epitaxy, the Si-face is therefore preferred.

Process conditions play a critical role in determining the quality of graphene. The number of graphene layers and their uniformity are primarily determined by the growth temperature, ambient pressure, and annealing duration, as these parameters control silicon desorption and carbon diffusion dynamics [122, 123, 125, 126]. Growth in high vacuum accelerates Si desorption, but can lead to nonuniform films [127], while argon-assisted growth slows the sublimation rate, improving layer uniformity and surface morphology [123, 125]. More advanced approaches, such as confinement-controlled sublimation [128, 129], face-to-face decomposition [130], and SiC-cap-assisted sublimation [131], regulate the local silicon partial pressure to achieve highly reproducible, large-area monolayer graphene. Surface preparation steps, including hydrogen etching [125, 127–129] and polymer pretreatment [132], are commonly used to reduce surface roughness and promote step-flow growth. To improve graphene flatness, a thermal shock annealing approach has recently been proposed [133]. By employing extreme peak temperatures with rapid heating and cooling, this method operates within a kinetic-limited growth regime, thereby suppressing step bunching.

A major advantage of SiC sublimation is that graphene is formed directly on an insulating or semi-insulating substrate, eliminating the need for a transfer process. Strong interfacial bonding between graphene and SiC, especially for the graphene buffer layer, ensures excellent thermal stability, enabling

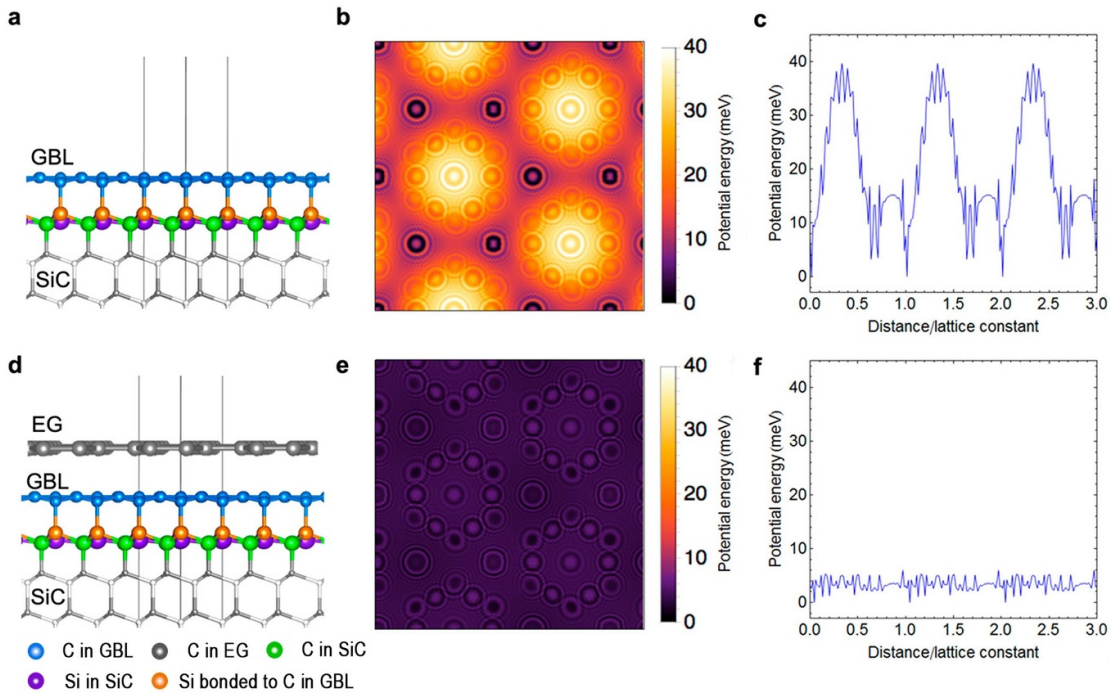

Figure 4. DFT simulations of electrostatic potential fluctuation across graphene on SiC. (a)–(c) Potential maps and line profiles for the graphene buffer layer. (d)–(f) Corresponding maps and profiles for EG grown on SiC. Reprinted with permission from [62]. Copyright (2021) American Chemical Society.

high-temperature processing with reduced interfacial degradation [62]. The close proximity of the graphene-substrate provides optimal conditions for efficient electrostatic field coupling (figure 4) [58, 62]. On the other hand, the graphitization process is inherently limited to SiC substrates, thereby restricting its broader applicability.

3.4. CVD growth

Compared to graphene produced by SiC sublimation, direct CVD offers greater flexibility and compatibility across a wider range of substrates. CVD-grown graphene also avoids polymer residues, reduces interfacial contamination, and eliminates mechanical damage associated with transfer-based techniques, driving interest in direct growth on substrates relevant to III-nitride technology [134–149].

Graphene-covered sapphire is especially attractive due to its thermal stability [150, 151] and intrinsic ionicity [60]. However, the low catalytic activity of sapphire requires activation of the carbon precursor, typically methane (CH_4). Metal-assisted approaches address this limitation by using deposited and annealed films of transition metal catalysts (typically, Cu or Ni) [137, 144, 145]. Carbon diffuses through the metal layer and nucleates at the metal-sapphire interface, forming a graphene monolayer. Afterwards, the metal film is removed by chemical etching [137, 144] or thermal shock [145], uncovering the graphene. This method offers a scalable route for integrating high-quality graphene with epitaxial templates. However, the additional steps required to remove the metal layers before device fabrication hinder its broader applicability.

To eliminate the etching step and avoid metallic contamination, catalyst-free CVD routes have been developed [134, 139, 146, 148, 149], enabling direct graphene growth on sapphire through alternative precursor activation mechanisms. The cracking of methane is enhanced at high temperatures, and graphene growth has been reported at temperatures reaching up to 1600 °C [134, 148]. However, such extreme temperatures deteriorate the substrate, and discontinuous films are obtained [148]. The growth temperature can be reduced by employing more reactive precursors, such as ethane (C_2H_6) [146] or diethylacetylene (C_6H_{10}) [139], or by using the plasma-enhanced dissociation of carbon precursors [149]. On the other hand, graphene grown at low temperatures typically exhibits nonuniform thickness owing to limited surface diffusion and excessive nucleation.

Direct graphene deposition on GaN and AlN templates using approaches similar to those developed for sapphire has also been reported [135, 136, 138, 142, 143]. Despite the progress, significant challenges remain in achieving the uniformity, crystallinity, and thickness control required for reliable remote epitaxy. Nonetheless, direct CVD growth offers a cleaner and more versatile alternative to transfer-based techniques, avoiding the substrate-specific limitations of SiC-derived graphene produced by sublimation.

3.5. Molecular beam epitaxy (MBE) growth

Graphene growth by MBE offers a transfer-free alternative to CVD-based synthesis and is attractive because it can, in principle, be integrated into all-MBE III-nitride process flows [82, 152, 153]. In a typical carbon MBE process, carbon is supplied under ultra-high vacuum from a heated graphite or pyrolytic-carbon source, an e-beam source, or a cracked precursor [153, 154]. Compared with CVD, MBE offers cleaner vacuum processing, precise control of carbon dose, and compatibility with straightforward in situ monitoring. However, because it lacks the catalytic metal chemistry that assists many CVD routes, the final carbon film depends strongly on the balance between carbon sticking, surface diffusion, desorption, substrate reaction or etching, nucleation, and lateral coalescence.

On non-metal templates, lower-temperature growth reports are usually graphene nanocrystals or graphitic carbon rather than continuous, high-quality graphene. For example, MBE growth on SiO_2 and mica produced layered graphene nanocrystals when the effective substrate temperature was approximately 500 °C and the carbon growth rate was kept low [155]. On Si (111), carbon deposition between 560 °C and 700 °C produced amorphous carbon or SiC-rich films, whereas graphitic carbon required an amorphous-carbon buffer followed by growth near 830 °C. Later Si-based studies used higher temperatures, around 820 °C–1000 °C [156–158].

For substrates directly relevant to III-nitride heteroepitaxy, the evidence remains limited. On $Al_2O_3(0001)$, mono- and few-layer nanocrystalline graphene has been reported at 800 °C–1000 °C, with higher temperature and longer deposition time improving crystallinity and continuity [152]. Single- and bilayer graphene have also been reported to grow at 1100 °C–1200 °C, but only within a narrow balance between carbon deposition and removal [159, 160]. Direct carbon MBE on GaN(0001) produced uniform graphitic carbon at approximately 900 °C [161]. Among nitride-relevant substrates, SiC remains the strongest case: carbon-face SiC can support graphene layers with preserved step-terrace morphology and graphene-like electronic structure, although rotational domains and thickness control remain important limitations [162].

Thus, MBE-grown graphene should be viewed critically for graphene-assisted III-nitride epitaxy. As an ideal remote-epitaxy interlayer, it is less mature than transferred graphene or EG formed by SiC sublimation, as it commonly yields nanocrystalline or defective carbon, with the strongest graphene-like results limited mainly to SiC [152, 159, 161, 162]. Nevertheless, this limitation may also be useful: thin sp^2-rich carbon layers can reduce adhesion, promote lateral adatom migration, and provide tunable nucleation sites. Recent work on ultrathin amorphous carbon supports this view, showing low-temperature sp^2-rich carbon layers as templates for MBE growth of high-quality cubic AlN and GaN on 3 C-SiC-based substrates [163]. Therefore, the near-term role of MBE-grown graphene or graphitic carbon is likely as a transfer-free, tunable carbon interlayer rather than as a fully established route to wafer-scale monocrystalline graphene templates.

4. Characterization of graphene prior to epitaxy

The structural and chemical qualities of transferred or grown graphene govern the nucleation and subsequent coalescence of nitride films. Structural continuity, interfacial cleanliness, and chemical stability directly influence the nucleation dynamics, lattice alignment, and exfoliation potential. Small-scale imperfections, such as vacancies or isolated pinholes, act as nucleation sites and will be discussed in the next chapter. Meanwhile, larger defects such as wrinkles, cracks, domain boundaries, or edge damage can trigger direct nucleation on the substrate, promote strain accumulation, and generate misoriented grains with different crystallographic orientations [27, 39, 62, 164–169].

Graphene can be characterized in situ during synthesis, most commonly during CVD growth on catalytic substrates. A review by Wang *et al* summarized the main approaches for monitoring nucleation, domain expansion, coalescence, catalyst reconstruction, chemical-state evolution, and interface formation in real time [170]. Representative capabilities are listed in table 2. Although these methods are especially valuable for identifying growth mechanisms, they usually require modified growth reactors. Therefore, for graphene templates used in III-nitride epitaxy, routine process control still relies mainly on post-growth, ex situ characterization.

Rapid, non-destructive ex situ characterization is typically performed using optical contrast methods and Raman spectroscopy. Optical microscopy, often enhanced by phase-sensitive imaging and reflectance mapping, is well suited for large-area screening and evaluation of layer-number uniformity, whereas Raman spectroscopy provides a more detailed probe of structural quality and local variations.

Optical microscopy offers a rapid, qualitative estimate of graphene thickness over large areas through contrast variations (figure 5) [179, 180]. Data-driven clustering and machine-learning classification of large-scale optical image datasets eliminate subjective judgment and reliably distinguish monolayer, bilayer, and trilayer graphene [181]. Phase imaging techniques, such as quadriwave lateral shearing interferometry, enhance optical contrast on transparent templates and provide direct measurements of both intensity and phase, enabling the accurate mapping of graphene thickness and optical constants [180].

Table 2. Representative in situ methods for monitoring graphene growth. The overview follows Wang *et al* [170].

Method	Information	Advantages	Limitations	Representative study
Optical microscopy, including radiation mode	Domain morphology, nucleation density, island size, and coalescence.	Enables real-time, large-area visualization and can be implemented close to practical CVD conditions.	Resolution is typically limited to the micron scale; high-temperature radiation and weak contrast can obscure small domains.	[171]
LEEM/LEED	Surface morphology, layer growth or etching, domain orientation, epitaxial registry, and reciprocal-space information.	Combines real-time surface imaging with crystallographic orientation information.	Usually requires UHV or low-pressure growth; the observation environment can differ from conventional reactors.	[172]
SEM	Nucleation rate, growth-front propagation, coalescence, etching, surface morphology with domain and surface evolution.	Provides higher spatial resolution than optical microscopy over mesoscopic fields of view and is useful for growth-rate analysis.	Gives limited chemical-state information unless combined with spectroscopy or diffraction.	[173]
TEM/STEM	Atomic lattice evolution, step-edge growth, defects, and local growth-front reconstruction.	Provides atomic spatial resolution that is inaccessible to optical or scanning-electron imaging.	Small field of view; electron-beam effects and specialized growth geometries can perturb the process.	[174]
STM	Carbon clusters, defective intermediates, carbide-to-graphene conversion, moire patterns, and local density of states.	Offers atomic-scale structural and electronic sensitivity to local growth intermediates.	Requires clean conductive surfaces and usually UHV; scans are slow and limited to small areas.	[175]
Raman spectroscopy	Evolution of the G, D, and 2D bands, including graphene formation, defects, layer number, stacking, and strain.	Non-destructive structural and quality probe that can provide real-time feedback during growth.	Weak signals can be masked by high-temperature blackbody radiation and reactor-window background.	[176]
XPS	Elemental composition, chemical states, carbide or intermediate species, dissolved carbon, and graphene-catalyst interaction shifts.	Chemically specific and able to distinguish carbon species that can look similar in imaging.	Spatially averaged and surface-sensitive; requires photon access and UHV or near-ambient-pressure-compatible setups.	[172]
XRR	Out-of-plane electron-density profile, interface roughness, and graphene–liquid-metal separation, quantifying interface evolution during growth.	Sensitive to buried interfaces and compatible with high-temperature liquid-metal growth environments.	Model-dependent and usually synchrotron-based; it does not identify chemical states by itself.	[177]
XRD	Catalyst phase, crystallinity, lattice evolution, and carbon-related diffraction peaks.	Gives robust phase and lattice information under reaction conditions and can be combined with spectroscopic probes.	Ensemble-averaged; weak graphene signals can be difficult to separate from catalyst diffraction.	[178]

For quantitative, layer-resolved imaging over large areas, reflectance mapping correlates optical reflectivity with thickness [182], and is particularly effective when integrated into micro-Raman systems for rapid screening of both crystalline and amorphous substrates.

Nevertheless, the applicability of optical contrast microscopy is strongly dependent on the underlying substrate. On SiO_2/Si substrates, graphene layer thickness can be identified via interference-enhanced optical contrast [179, 183]. For SiC substrates, optical microscopy, reflectance mapping, and confocal laser scanning microscopy have been employed to distinguish EG domains and determine layer number [182, 184, 185]. In contrast, for substrates such as sapphire, GaN, and AlN, optical microscopy is primarily limited to rapid inspection of surface coverage, wrinkles, cracks, and overall uniformity, while accurate determination of layer number typically requires complementary techniques [135, 138, 142, 145, 186]. Consequently, on these substrates, optical contrast microscopy should be regarded mainly as a preliminary screening tool unless substrate-specific calibration is performed.

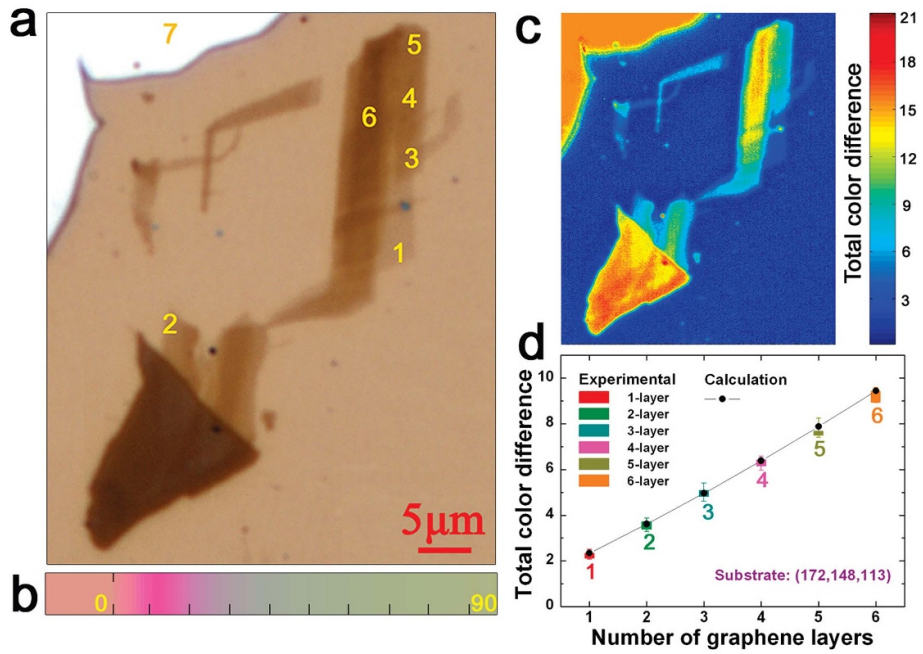

Figure 5. (a) Optical image of graphene transferred onto a Si wafer. Areas with distinct optical contrast are marked as regions 1–7.(b) Calculated color reference for graphene. (c) Map of experimentally extracted color difference across the field of view in (a), obtained by converting the measured RGB values. (d) Theoretical color difference values versus graphene thickness compared with experimental at sites 1–6 in (a). Reprinted with permission from [179]. Copyright (2008) American Chemical Society.

Raman spectroscopy is the most widely used and reliable method for assessing graphene thickness and crystalline quality (figure 6) [187–189]. The key features of the graphene Raman spectrum include the *G* band (∼1582 cm^{-1}), arising from the in-plane optical phonon (E_{2g} mode) associated with the stretching vibration of two neighboring sp^2 carbon atoms, and the 2D band (∼2700 cm^{-1}, strongly dispersive with the excitation energy, also referred to as the *G′* band), a second-order double-resonant feature involving two intervalley TO phonons near the *K* point. In defective graphene, the defect-activated *D* band (∼1350 cm^{-1}, strongly dispersive with excitation energy) arises from a vibrational pattern in which a carbon atom hexagon expands and contracts uniformly and is activated by intervalley double-resonant scattering that transfers an electron between inequivalent *K* and *K′* valleys via a TO phonon near the zone edge. A related intravalley process produces the *D′* band (∼1620 cm^{-1}), which often overlaps with the *G* band.

The Raman features of graphene are highly sensitive to the layer thickness and defect density, making Raman spectroscopy especially valuable for evaluating graphene quality and lattice damage introduced during synthesis, transfer, or post-processing. In monolayer graphene, linear electronic dispersion yields a single dominant resonant scattering path, producing a sharp, symmetric 2D peak that is more intense than the *G* peak, typically by a factor of 2–4 [190]. Increasing the number of layers introduces interlayer coupling that modifies the electronic bands near the *K* point, creating multiple resonant channels, and leads to broadening and splitting of the 2D band, thereby reducing its intensity relative to the *G* band [187–189]. The intensity ratio I_{2D}/I_G is commonly used as a fingerprint of graphene thickness [101, 103, 104, 113, 119, 124, 133, 134, 136, 137, 141, 144–149, 165, 169]. Likewise, the relative intensity of the defect-induced D band provides a measure of structural quality through the ratio I_D/I_G [82, 101, 104, 111, 114, 119, 133, 134, 138, 140–144, 146–149, 165, 169].

However, Raman analysis of graphene on SiC or III-nitride-related substrates requires substrate-specific considerations. Both SiC and GaN substrates exhibit second-order Raman features in the ∼1000–2000 cm^{-1} range, which can overlap with the graphene *D* and *G* bands, often requiring substrate background subtraction [124, 191–193]. Moreover, strain, charge transfer, and buffer layer coupling can induce shifts in the *G* and 2D bands [124, 191, 193]. In GaN, these second-order contributions may further depend on the excitation wavelength and substrate quality [192, 193]. In contrast, sapphire introduces minimal spectral overlap with graphene Raman features [194, 195]. However, graphene peak positions, FWHM values, and intensity ratios can still reflect substrate coupling, strain/doping, and transfer-related residues [145, 195–197]. Consequently, Raman spectroscopy remains a highly useful tool for the characterization of graphene on III-nitride-related templates. However, quantitative analysis of layer number and defects should incorporate

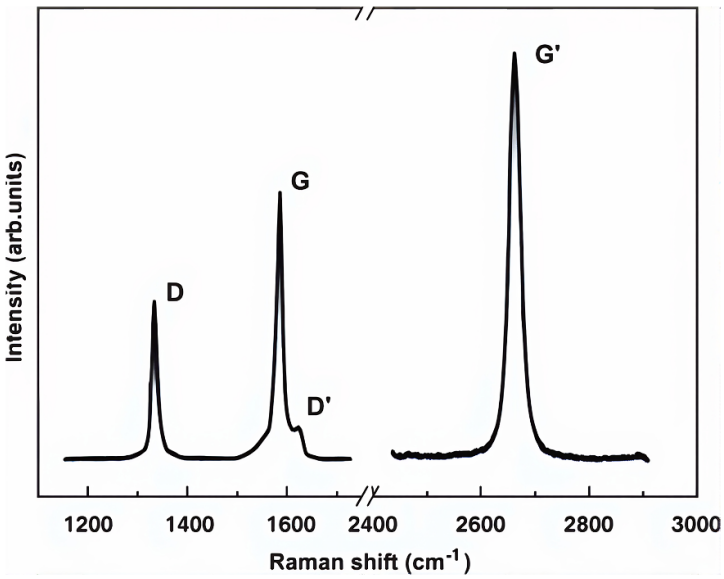

Figure 6. Raman spectra of monolayer graphene showing *G*, 2D, *D*, and *D′* bands. These features provide insight into layer number, doping, and structural disorder. Reprinted from [187], Copyright (2009), with permission from Elsevier.

background subtraction and complementary techniques where appropriate.

Optical characterization methods are complemented with electron microscopy techniques. Scanning electron microscopy (SEM) imaging (figure 7 Top) provides contrast-based estimates of graphene thickness [198]: the contrast arises from the attenuation of the secondary electron yield with increasing graphene thickness. SEM also enables direct observation of mesoscale features such as wrinkles, tears, cracks, and grain boundaries [199, 200]. For atomic-scale resolution, high-resolution transmission electron microscopy (TEM) (figure 7 Bottom) directly visualizes graphene layers and interlayer spacing. Although typically reserved for post-growth analysis due to the destructive nature of sample preparation, TEM is essential for confirming the preservation of graphene layers beneath epitaxial films and for detailed interfacial characterization [60, 146, 201, 202]. Atomic force microscopy (AFM) can additionally be used to measure graphene layer thickness, assess wrinkle density, and, crucially, evaluate surface adhesion [203–205], while high-resolution surface-chemical methods such as x-ray photoelectron and time-of-flight secondary ion mass spectroscopy provide chemical characterization and quantify residues, together enabling a comprehensive pre-growth assessment [206].

5. Graphene-assisted growth of III-nitrides

A key bottleneck in graphene-assisted III-nitride epitaxy arises from the coupling between graphene preparation and subsequent nitride growth. Graphene transfer or direct growth methods define the initial defect and contamination landscape, while high-temperature MOCVD nucleation and coalescence can amplify these nonuniformities, degrade the graphene layer, or induce local chemical anchoring [207–210]. Consequently, achieving reproducible, high-quality nitride growth requires not only improved graphene integration but also careful control of early-stage growth processes to preserve structural uniformity and interfacial integrity.

Early-stage nucleation events govern the growth mode, defect density, and crystallographic alignment of epitaxial films. In conventional heteroepitaxy, morphology is determined by surface and interfacial energies, elastic strain energy, supersaturation, and adatom diffusion length. Depending on these factors, growth can proceed by 2D layer-by-layer growth (Frank–van der Merwe), step-flow growth on vicinal surfaces, 3D islanding (Volmer–Weber), strain-driven wetting-layer-plus-island growth (Stranski–Krastanov), or mixed island/coalescence/step-flow pathways [211, 212]. Step-flow becomes more favorable when adatom mobility is high and terraces are well defined, whereas low mobility or high supersaturation promotes terrace nucleation and island formation. This balance underlies the common two-step GaN growth strategy, where low-temperature nucleation is followed by high-temperature lateral coalescence [213]. Nucleation on graphene faces a higher energy barrier and therefore requires elevated supersaturation or intentionally engineered nucleation sites [23, 60, 214, 215]. The growth front can switch between weakly coupled and defect-anchored pathways, depending on local interfacial chemistry and graphene integrity. Consequently, the transition from isolated III-nitride nuclei to a closed film on

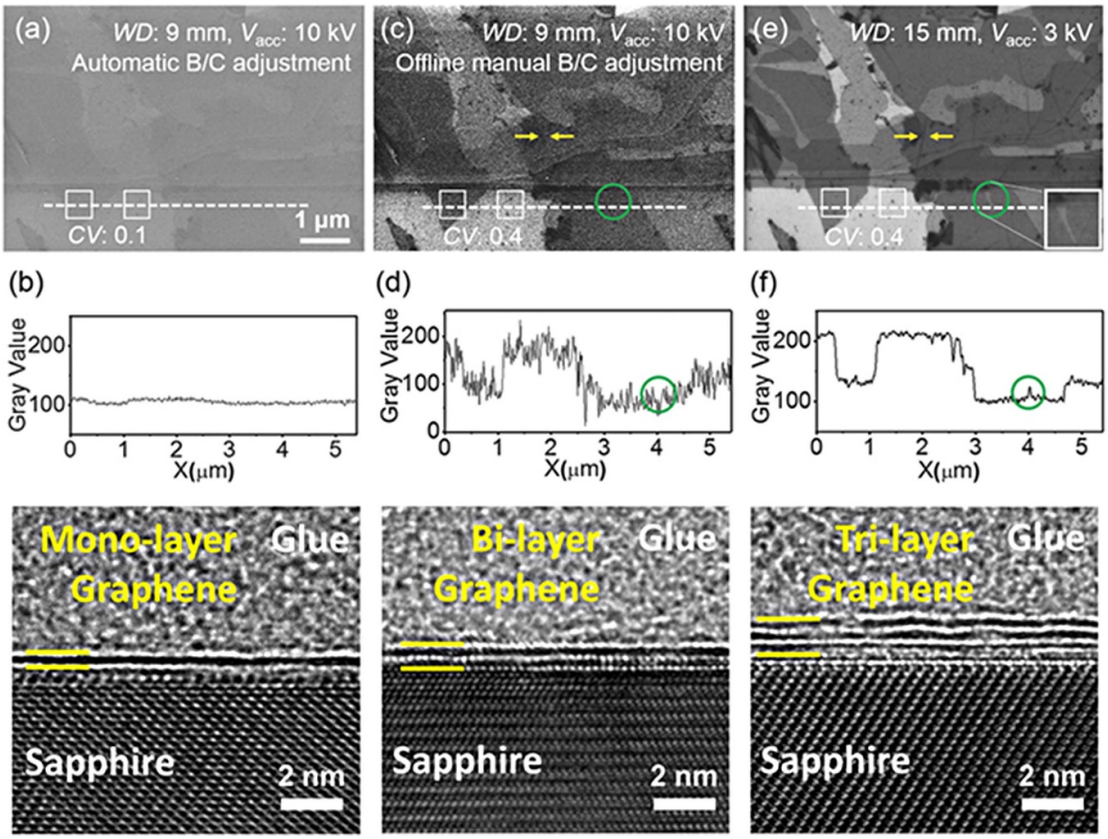

Figure 7. Graphene characterization using electron microscopy. (Top) SEM contrast images of graphene on SiC under tuning V_{acc} and working distance conditions, with (Middle) the line profile of gray-scale values along the white line. [198] John Wiley & Sons. © 2018 WILEY-VCH Verlag GmbH & Co. KGaA, Weinheim. (Bottom) Cross-sectional high-resolution TEM images of mono-, bi-, and trilayer graphene synthesized via sequential CVD growth cycles. Reprinted with permission from [146]. Copyright (2022) American Chemical Society.

graphene-covered templates should be viewed as a local mixture of weakly coupled and defect-anchored pathways, requiring both a laterally uniform density of stable nuclei and efficient lateral/step-flow coalescence while preserving the continuity of the graphene interlayer.

5.1. Growth initiation by defects

Pristine graphene is chemically inert and provides few reactive adsorption sites. Hence, III-nitride nucleation on an intact graphene surface is intrinsically difficult and typically yields a low density of stable nuclei [47, 64, 164, 216–221]. The relatively high ratio of adsorption energy to bulk cohesive energy (reported to be close to 0.97 for GaN in one analysis [42]) suggests a tendency toward 2D growth once a sufficiently dense nuclei population is established. However, this ratio is best interpreted as a comparative metric within the same computational framework, rather than as a universal wetting criterion. The weak interaction at the vdW interface can reduce the interfacial locking, limiting the short-range registry during early-stage growth and leading to rotational disorder or polycrystalline films [12, 64, 201, 222]. On the other hand, this weak coupling is also advantageous: it decouples the epilayer from the underlying template, which can facilitate strain relaxation and, in favorable cases, subsequent release [14].

Enhancing the surface chemical activity of graphene increases the nucleation density and potentially improves crystalline quality [38, 64, 220, 223, 224]. Various modification strategies [225], including oxygen plasma treatment [47, 209, 222], fluorination [226, 227], nitrogen plasma exposure [38, 64, 164], hydrogenation [228–230], and ammonia treatment [27, 169, 231], have been employed to functionalize the graphene surface. Modifying the graphene surface chemistry shifts the growth from an ideal remote/vdW toward defect-mediated regimes such as QvdW or thru-hole epitaxy [60, 64]. In these cases, the interface is best described as a hybrid: nucleation is initiated at discrete defects where localized covalent bonding can form, whereas lateral expansion and overgrowth proceed across adjacent intact graphene regions through weak vdW coupling [23, 64, 232, 233]. This mixed pathway naturally produces spatial heterogeneity, because regions seeded by strong anchoring sites evolve differently from areas where nucleation is sparse (figure 8).

A clear illustration is provided by the GaN growth on patterned graphene/GaN templates, where two

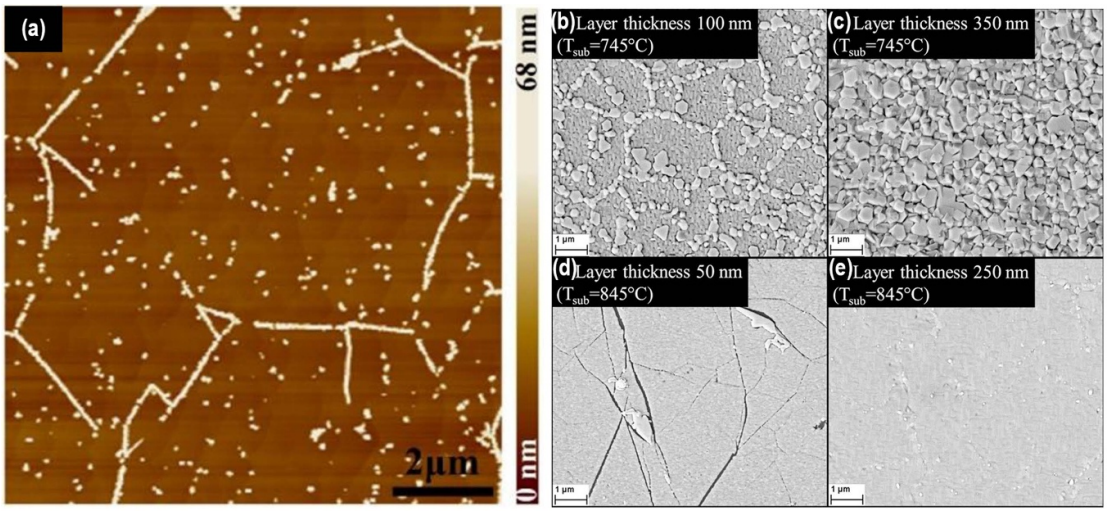

Figure 8. Nucleation and early coalescence on graphene-covered templates. (a) AFM image of AlN nuclei aligned along line-like trajectories on CVD-grown bilayer graphene, consistent with defect-guided nucleation. Reprinted with permission from [169]. Copyright (2025) American Chemical Society. (b)–(e) SEM images of GaN grown on graphene/3 C-SiC: growth at 745 °C yields polycrystalline morphology with visible line-like trajectories with higher nucleation density, whereas growth at 840 °C improves phase purity and increases thickness. Scale bars: 1 μm. [168] John Wiley & Sons. © 2023 The Authors. physica status solidi (b) basic solid state physics published by Wiley-VCH GmbH.

distinct nucleation and early growth modes have been reported [234]. In the microwindow regions without graphene, GaN nucleates at the step edges on both sides of the exposed GaN openings, then grows laterally and merges into continuous overgrowth strips [234]. In parallel, nucleation on the graphene mask occurs primarily at defect sites such as wrinkles and nano-holes, leading to localized island growth [234]. Islands associated with wrinkles remain small and show weak crystallographic alignment, whereas islands nucleated at nano-holes are larger and exhibit a consistent orientation [234]. Although these islands largely preserve the substrate-determined orientation, their impingement behavior differs from that in the window regions, leading to discontinuous coverage over the graphene mask (figure 9).

Additional insights into how defects activate nucleation come from plasma-assisted MBE A dedicated study showed that GaN nucleation on graphene is not spontaneous but is triggered after nitrogen-plasma exposure, which generates vacancies and pinholes and incorporates nitrogen into the graphene lattice [235]. The resulting N-incorporated configurations served as adsorption/anchoring centers for Ga adatoms, thereby facilitating Ga–N bond formation. Notably, the authors observed that MBE-grown nanostructures were more resistant to mechanical displacement than MOCVD-grown islands, consistent with stronger local interfacial bonding, and therefore, a larger contribution from defect-anchored nucleation under plasma conditions [235].

Functionalization enhances nucleation on graphene and can therefore enable the epitaxial growth of otherwise difficult-to-integrate 3D nitrides, such as GaN and AlN, on 2D templates [23, 56, 164, 214]. However, if functionalization is accompanied by substantial structural damage, including cracks and domain boundaries, the resulting nonuniform interfacial chemistry can promote polycrystalline regions and trigger local changes in the growth mode [17, 29, 166].

5.2. Nucleation and coalescence

Graphene-assisted III-nitride epitaxy has been demonstrated on diverse templates, including graphene-covered III-nitrides, sapphire, SiC, Si-based, and amorphous substrates [26, 29, 210, 236]. Both MOCVD and MBE are used on these platforms. MBE provides a comparatively cleaner, low-temperature environment ideal for preserving interface quality and testing remote epitaxy concepts [16, 28]. MOCVD, by contrast, is a more industrially viable option. However, it operates under chemically aggressive, high-temperature conditions, where epitaxial growth is strongly influenced by interfacial defects and reactor-specific parameters.

For clarity, reports of continuous III-nitride films grown by MOCVD on graphene-covered templates can be grouped into three process archetypes: (1) single-step high-temperature growth (without a dedicated low-temperature nucleation step), (2) two-step growth separating nucleation and coalescence into distinct temperature windows, and (3) pulsed-driven schemes that modulate the precursor supply and diffusion during coalescence. In the following sections, we discuss the preparation of graphene, key stability constraints, nucleation pathways, and coalescence on common III-nitride epitaxial platforms.

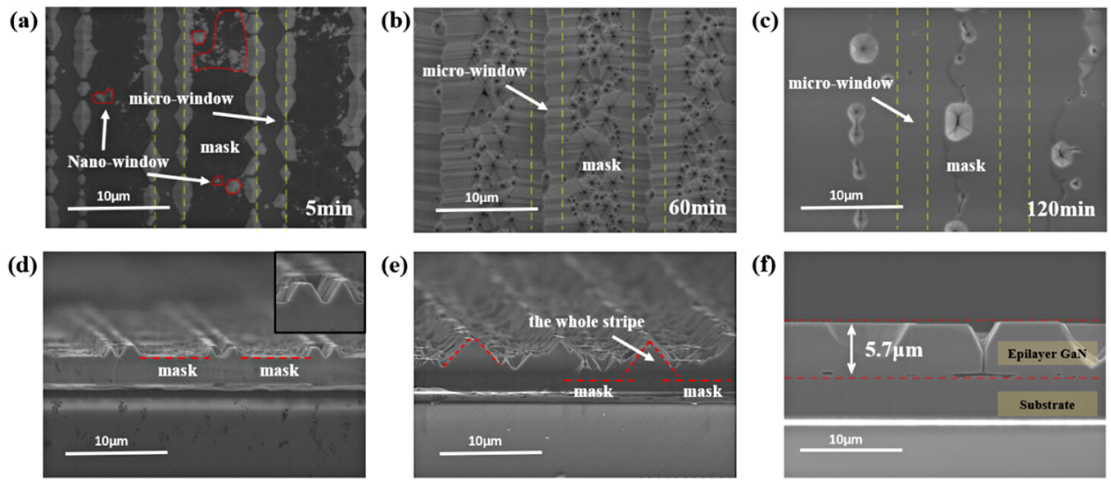

Figure 9. Top-view and cross-sectional SEM images of GaN grown on patterned graphene/GaN templates. Panels (a)–(c) show plan views after 5, 60, and 120 min of growth; (d)–(f) show corresponding cross-sections. The inset in (d) highlights island morphology at early growth stages. Reprinted with permission from [234]. Copyright (2023) American Chemical Society.

5.2.1. Native nitride templates

Remote homoepitaxy is attractive because it combines the benefits of a homoepitaxial registry with the potential to produce films that can be exfoliated as thin membranes. For this reason, graphene-coated native nitride templates have been widely studied under MOCVD conditions [39, 167, 207, 208, 237–243]. Native nitride substrates exhibit relatively strong electrostatic surface fields (section 2.3), which can penetrate thin graphene and influence nucleation. As a result, guided crystalline registry of the overgrown epilayer can be achieved when the graphene interlayer is sufficiently thin, typically $\lesssim$3 layers [58]. However, achieving this behavior in practice is highly sensitive to interface quality, and it cannot be reliably obtained without careful control of the graphene thickness uniformity, defect density, and process chemistry.

Graphene-covered templates exhibit substrate- and temperature-dependent stability windows that strongly affect nucleation behavior and, ultimately, the feasibility of film exfoliation [151, 208, 237, 239, 240]. A key challenge with native nitride templates is degradation caused by thermal stress and chemical reactions between graphene, the growth ambient, and the underlying surface [151, 167, 207, 208, 239, 241, 244]. Nitride surface volatility under H_2- and NH_3-containing ambients can accelerate graphene etching and defect formation, and in severe cases, lead to loss of the interfacial layer. Annealing studies confirm that degradation accelerates with temperature and is most severe under hydrogen-rich conditions [151, 239, 245] (figure 10).

Graphene on GaN begins to degrade at temperatures as low as 800 °C [240] even in N_2 atmosphere [237, 239]. Degradation is evidenced by the emergence of disorder-activated D and D' bands in the Raman spectra, indicating increased sp^3 bonding, along with the loss of sharp G and 2D peaks, as shown in figure 10. The process begins when nitride templates decompose at high temperatures and release nitrogen species that react with graphene [151, 245]. Rapid thermal cycling further promotes microcrack formation [246], especially along pre-existing wrinkles, accelerating degradation and compromising exfoliability [151, 207].

AlN substrates, while not immune to degradation, exhibit greater thermal resilience than GaN [241]. The delayed onset of nitrogen outgassing makes AlN more suitable for preserving graphene during high-temperature MOCVD [245, 247, 248]. Thus, the stronger dipole field and higher thermal stability of AlN make it a more favorable candidate for maintaining the graphene functionality and initiating successful remote epitaxy.

Despite these stability constraints, low-temperature buffer layers can still be deposited on the graphene. For example, GaN buffers grown on graphene-covered AlN/sapphire templates at 580°C–800°C using N_2 as the carrier gas preserved the graphene interlayer and enabled successful exfoliation. In contrast, increasing the temperature to 850°C or using H_2 as the carrier gas compromised the integrity of the graphene layer, which ultimately prevented successful exfoliation [240]. At lower temperatures, GaN nucleated as misoriented 3D islands on the inert graphene surface and did not fully coalesce into a smooth layer. Moreover, GaN grown at lower temperatures may adopt mixed or metastable phases, resulting in lower crystalline quality [249], complicating the optimization of epitaxial conditions.

Despite evidence of graphene degradation in harsh environments, the single-step high-temperature process has been implemented [64]. The drawbacks of a high-temperature growth step

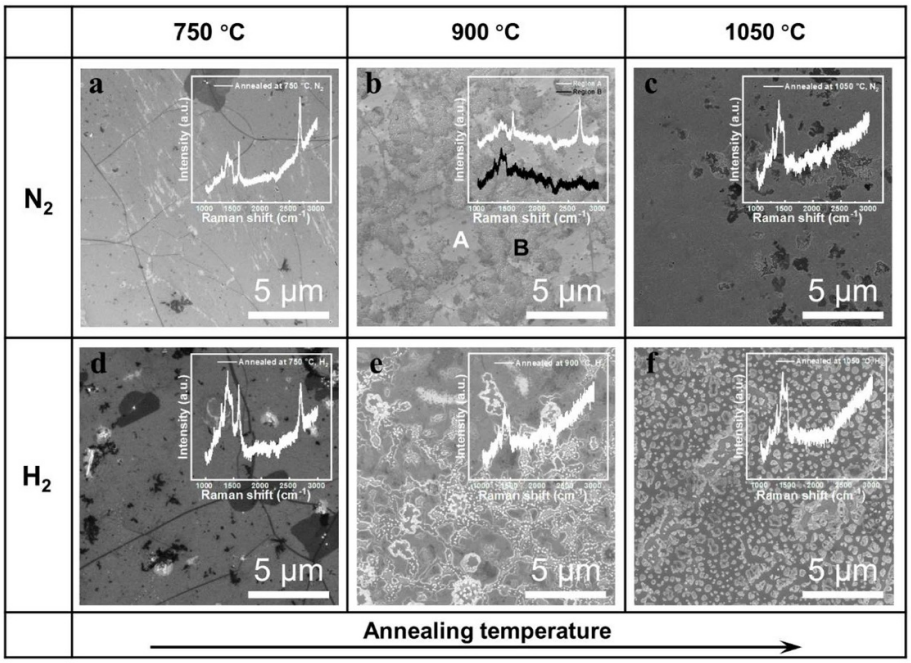

Figure 10. Graphene-covered GaN templates annealed at different temperatures and atmospheres. (a)–(c) SEM images and Raman spectra after annealing at 750 °C (a), 900 °C (b), and 1050 °C (c) in N_2; (d)–(f) corresponding conditions in H_2. [239] John Wiley & Sons© 2022 Wiley-VCH GmbH.

are most evident on transferred graphene, where polymer residues, wrinkles, and spatially varying defect densities can lead to highly nonuniform nucleation. On wet-transferred graphene/AlN templates, MOCVD growth at 1000 °C in H_2 produced continuous III-nitride layers. However, without additional surface treatment, the films remained polycrystalline and exhibited strong in-plane twisting. In the same work, deliberate interface functionalization via atomic nitrogen exposure in an MBE chamber enabled QvdW epitaxy, yielding a higher crystallinity AlN film with a single in-plane orientation under otherwise identical MOCVD conditions [64]. Mechanistically, remote interactions transmitted through graphene can enforce polarity inheritance but provide insufficient constraints to suppress thermally accessible in-plane rotations. Introducing localized covalent bonding at engineered sites adds an explicit registry condition that reduces rotational degeneracy as islands coalesce (figure 11).

On native nitride templates, a single high-temperature MOCVD step is generally unfavorable for graphene-assisted growth. At high temperatures, both adatom mobility and desorption rates increase significantly. On pristine graphene, where the nucleation barrier is already high, this combination can lead to a very low island density. Consequently, there is a higher likelihood that graphene will degrade before a continuous layer can be formed. As a result, two-step growth schemes are commonly adopted. A low-temperature nucleation stage increases the probability of forming stable nuclei by improving the adatom sticking, suppressing desorption, and increasing the likelihood of preserving the graphene interlayer. A subsequent high-temperature step then promotes lateral overgrowth and improves crystalline quality by enabling defect reorganization/annihilation and reducing point-defect incorporation.

Numerous studies have shown that two-step MOCVD mitigates some limitations of single-step growth on graphene, but does not eliminate the key challenges [207, 237, 241, 242]. This approach was extended to both low-temperature GaN and AlN buffers on graphene-covered AlN/sapphire in a study examining the effects of post-growth annealing at 1045 °C [241]. After graphene transfer and annealing in N_2 or H_2, the Raman spectra showed better graphene preservation in N_2 ($I_D/I_G \sim 0.95$) than in H_2 ($I_D/I_G \sim 1.12$). Subsequent GaN buffer growth at 800 °C for 15 min maintained graphene integrity and enabled exfoliation. However, even a brief 1 min annealing at 1045 °C irreversibly degraded graphene. EDS revealed carbon depletion at the interface, and TEM showed conversion from sp^2 to C–N bonding (figure 12). The SEM images of the recrystallized films indicate grain boundary densification after annealing. Similar results were observed for the AlN buffer.

Despite repeated reports of graphene degradation and incomplete release, two-step MOCVD on native templates is still being employed. However, the benefits of exfoliation and crystalline registry have been overlooked. The lack of a crystalline registry was well represented on graphene-covered AlN/sapphire templates, where GaN nucleation was initiated at

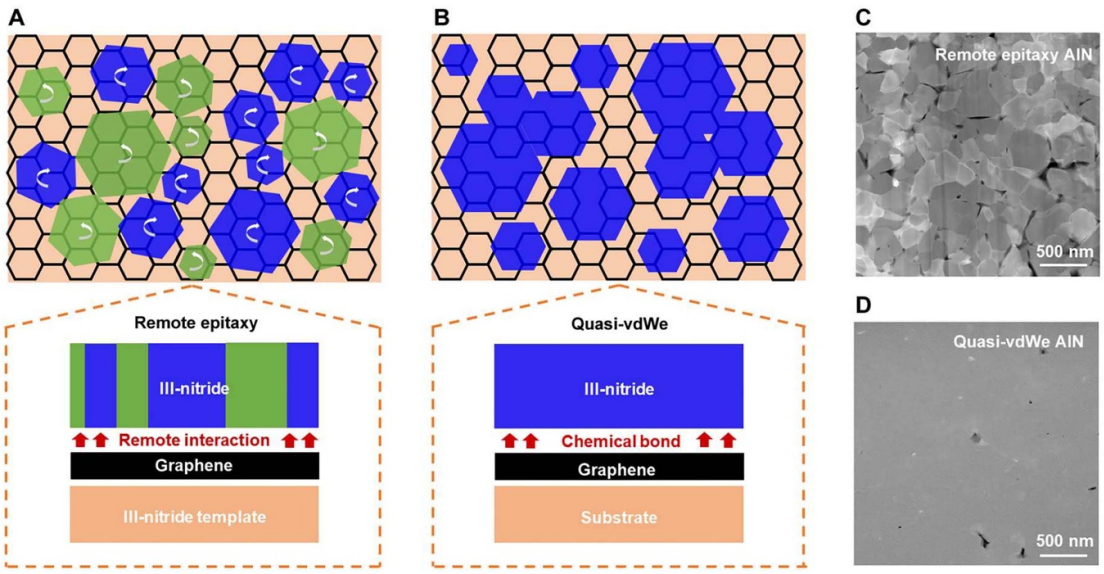

Figure 11. Comparison of AlN epitaxy on (A) and (C) unfunctionalized and (B) and (D) functionalized graphene. QvdW epitaxy, facilitated by defect-mediated nucleation on transferred graphene, improves grain alignment relative to remote-epitaxy-like growth. From [64]. Reprinted with permission from AAAS.

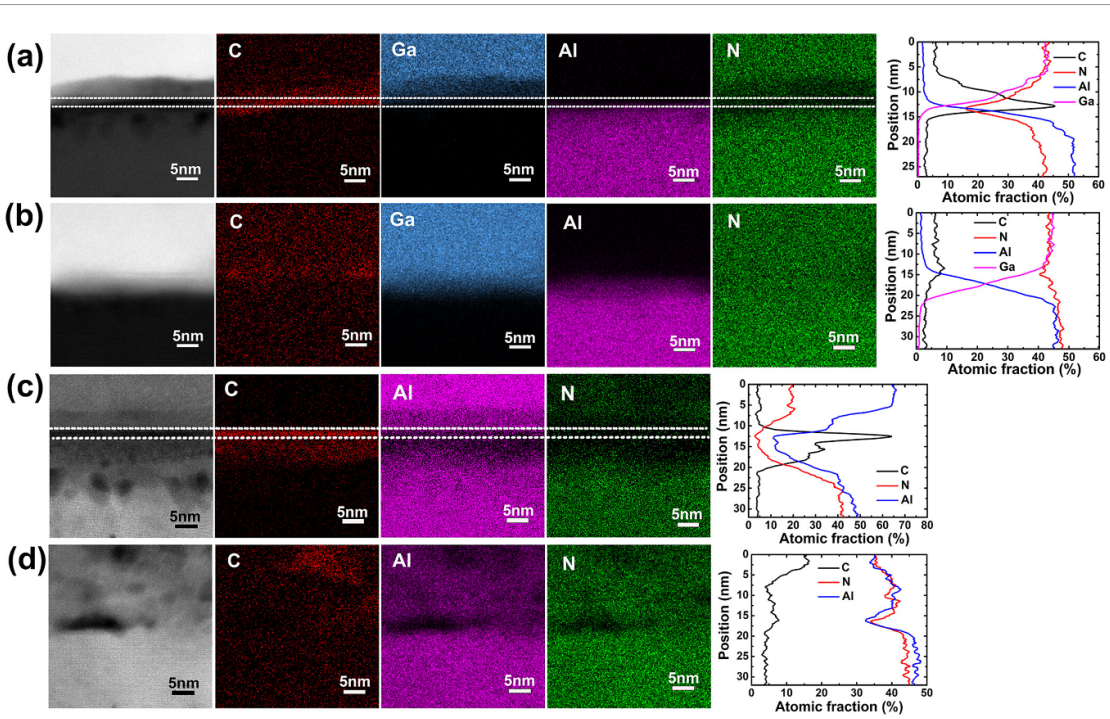

Figure 12. Cross-sectional TEM, EDS maps, and carbon fraction profiles for (a) GaN buffer without anneal, (b) GaN buffer with anneal, (c) AlN buffer without anneal, and (d) AlN buffer with anneal. The presence or absence of graphene highlights the effect of high-temperature processing. Reprinted with permission from [241]. Copyright (2023) American Chemical Society.

750 °C for 10 min, followed by a high-temperature lateral overgrowth step at 1050 °C for 60 min [207]. In the early stage, GaN formed hexagonal islands that exhibited an in-plane registry with the underlying AlN, indicating crystallographic transmission across the graphene interlayer (figure 13). However, diffraction analysis showed broader rocking curves than those for GaN grown directly on AlN, consistent with higher mosaicity and an elevated defect density in the coalesced film (figure 14) [207]. Importantly, the high-temperature step exposed a practical failure mode: nanoscale pits in the AlN template locally destabilized the graphene, enabling direct GaN-AlN contact. This mixed interface increased the interfacial pinning and ultimately impeded exfoliation [207].

Moving from graphene-covered AlN to graphene-covered GaN templates further narrows the graphene stability window and is often accompanied by

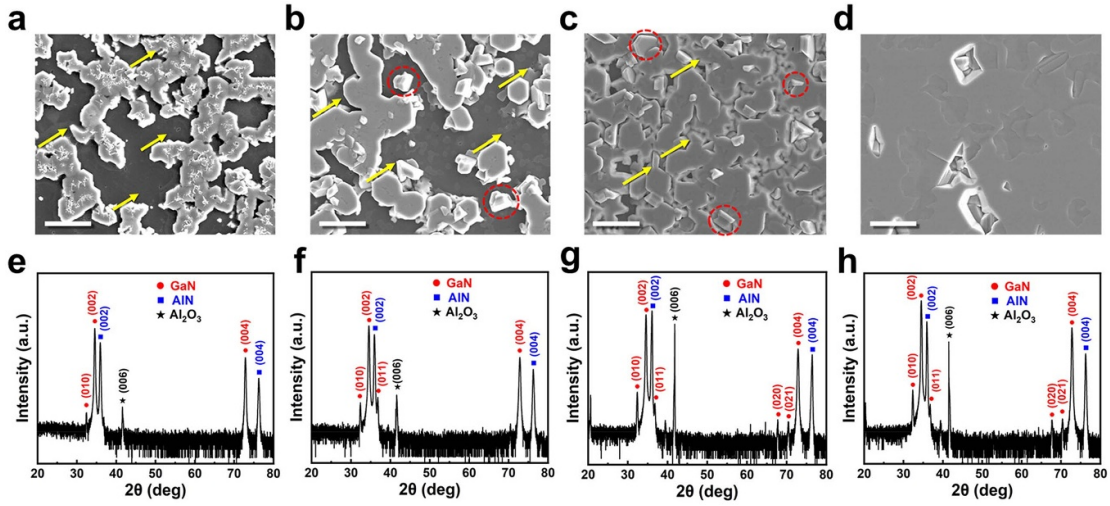

Figure 13. Surface evolution and structure of GaN grown on graphene/AlN as a function of growth time. Results are shown after the initial GaN deposition (a) and (e), and after the second GaN growth step for 5 min (b) and (f), 10 min (c), (g), and 60 min (d) and (h). The SEM and XRD measurements capture the progression from discrete nuclei to a nearly continuous GaN layer, accompanied by an increase in diffraction intensity and the emergence of partial in-plane orientational ordering with extended growth. Scale bars in images (a)–(d) correspond to 4 μm. Reprinted with permission from [207]. Copyright (2023) American Chemical Society.

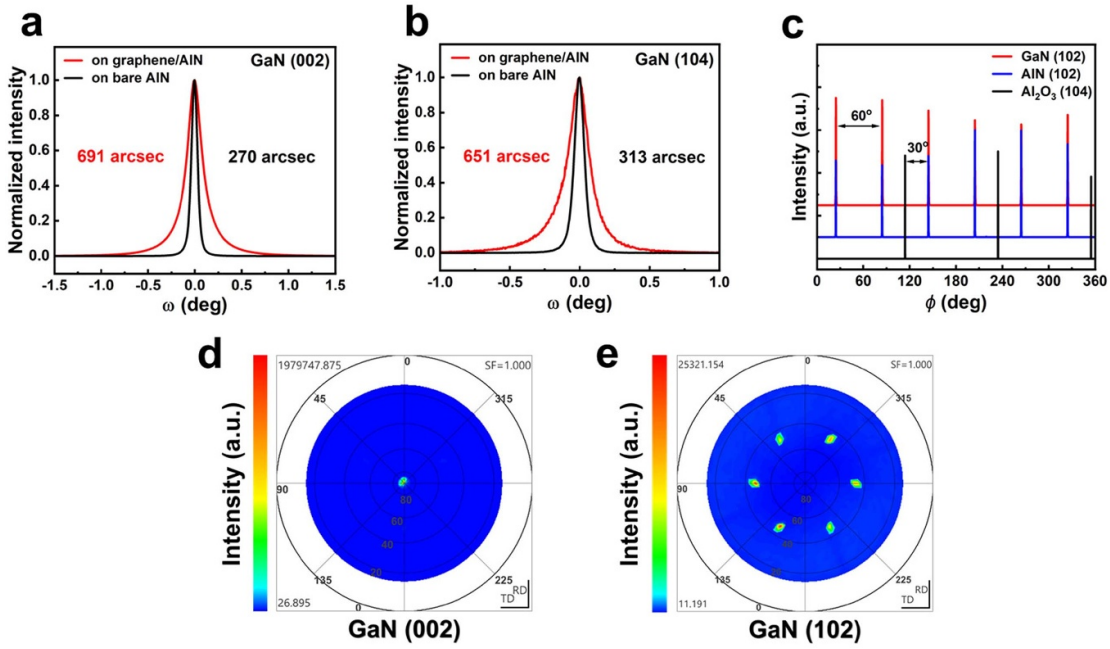

Figure 14. XRD characterization after the second GaN regrowth. (a) ω-rocking curves of the GaN (002) reflection grown on graphene/AlN and on an AlN control. (b) ω-rocking curves of the GaN (104) reflection for the same two templates. (c) Azimuthal (ϕ) scan of GaN on the graphene/AlN template demonstrating in-plane registry. (d) and (e) Pole-figure measurements for the GaN (002) and (102) reflections, respectively. Reprinted with permission from [207]. Copyright (2023) American Chemical Society.

increased polycrystallinity and a lack of coherent in-plane orientation in the overgrown GaN [242]. To reduce polycrystallinity while retaining exfoliation capability, a defect-engineering route was introduced in which graphene/GaN templates were annealed at 900°C in N_2, inducing partial GaN surface decomposition and nitrogen incorporation into graphene [239]. The resulting self-organized defective graphene interlayer supported dual-mode nucleation. Using an initial growth step at 900 °C followed by high-temperature growth at 1050 °C, 1.5 μm-thick GaN films were obtained with a surface roughness of ∼0.26 nm. Rocking-curve analysis indicated reductions of 51% and 62% in screw and edge dislocation densities, respectively (figure 15). Raman spectroscopy further suggested reduced residual

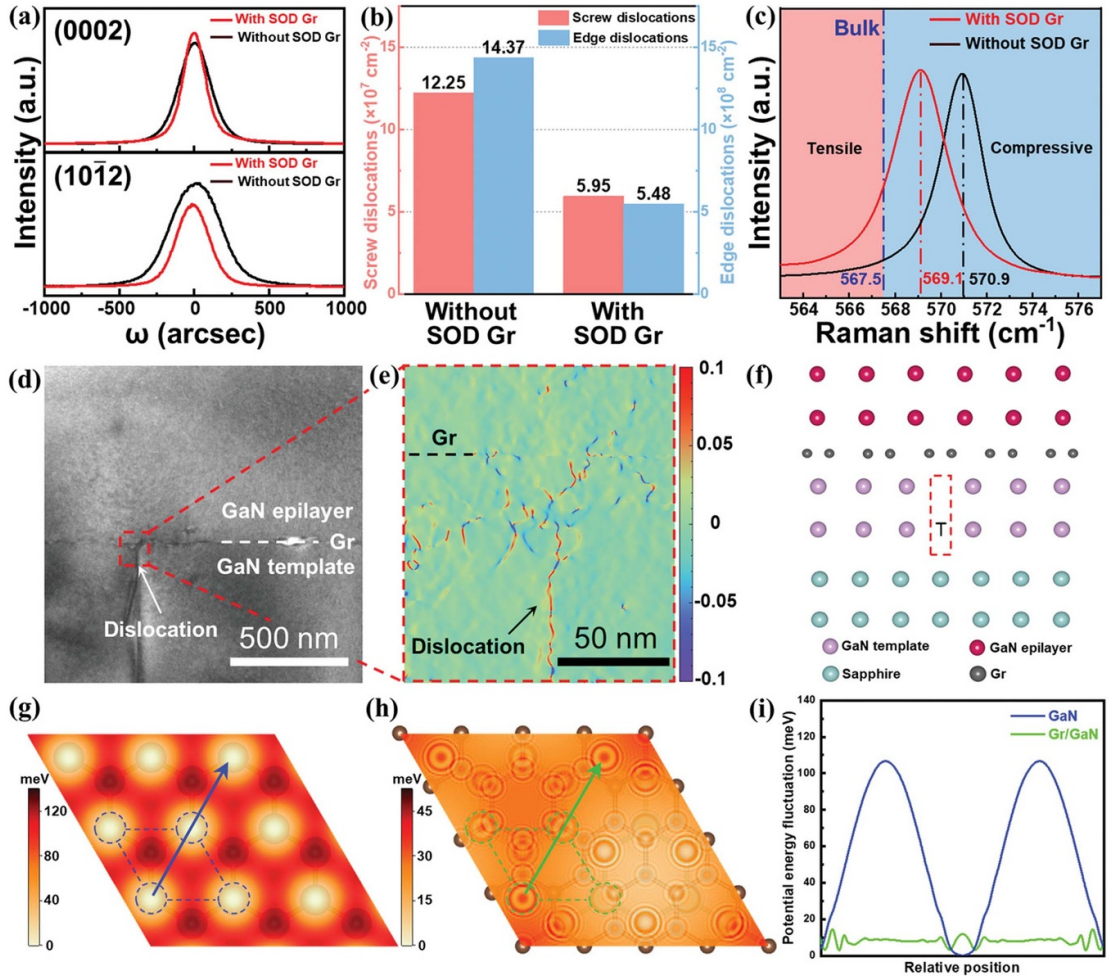

Figure 15. Dislocation behavior and strain relaxation enabled by a GaN/graphene interface. (a) x-ray rocking curves of the GaN (0002) and (10$\bar{1}$2) reflections for epilayers grown on GaN templates with (red) and without (black) graphene interlayer; (b) screw and edge dislocation densities extracted from these widths. (c) Raman E_2 phonon spectra showing residual strain. (d) Dark-field TEM image of the GaN epilayer/graphene/GaN template and (e) corresponding geometric phase analysis of e_{xx} strain map near an interfacial dislocation. (f) Conceptual sketch illustrating dislocation blocking via interfacial sliding at graphene. (g) and (h) DFT-derived surface potential fluctuation maps for bare and graphene-covered GaN, with (i) line profiles indicating diminished potential variations for the graphene-covered surface. [239] John Wiley & Sons© 2022 Wiley-VCH GmbH.

biaxial strain, and cross-sectional TEM showed the termination of threading dislocations at the defective graphene interlayer [239].

Maintaining the integrity of large-area graphene during nucleation is critical for successful exfoliation and can limit the applicability of graphene-assisted MOCVD at high temperatures on native templates. Remote epitaxial registry under MOCVD conditions is difficult to achieve on native nitrides due to template instabilities. The effective stability window also depends on substrate polarity: monolayer graphene on N-polar surfaces exhibits higher thermochemical stability than that on Ga-polar surfaces [60]. Under conditions where graphene remains intact, increasing the temperature tends to decrease the nucleation density while increasing the size of GaN microcrystals, consistent with the enhanced adatom mobility and longer diffusion lengths on undamaged graphene.

This polarity dependence may be advantageous for HEMT-oriented integration, as N-polar designs can exploit the reversed polarization field to provide a natural back-barrier, stronger carrier confinement, improved gate control, and lower access/contact resistance compared with conventional Ga-polar architectures [250]. Recent N-polar GaN-on-sapphire deep-recess HEMTs and high-uniformity 100 mm N-polar HEMT processes have demonstrated strong W-band power density and efficiency, suggesting that graphene-assisted approaches preserving N-polar surfaces could be valuable for releasable or heterogeneous RF devices [251, 252].

Overall, although low-temperature buffer strategies can mitigate some limitations, high-temperature processing can still cause irreversible graphene degradation and restrict large-area remote-epitaxy implementations on native templates [241]. As a result, defect-mediated pathways (QvdW or thru-hole

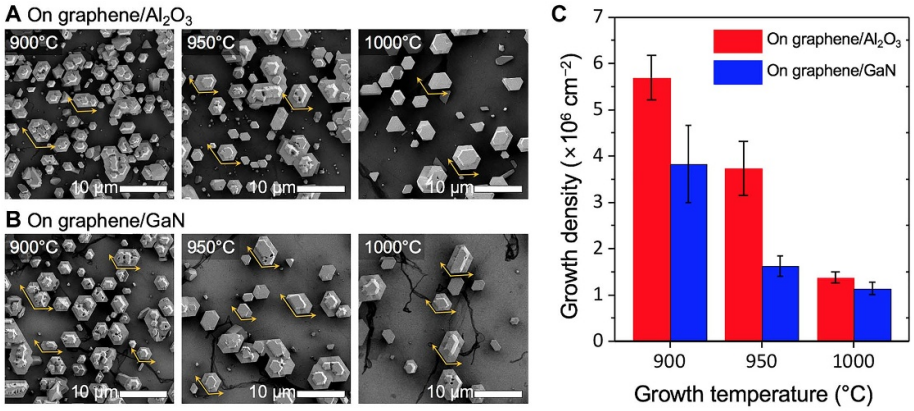

Figure 16. The influence of substrate ionicity and growth temperatures on the formation of GaN microcrystals. SEM images show nucleated GaN microcrystals on (A) graphene/Al_2O_3 and (B) graphene/GaN templates, along with their corresponding nucleation temperatures. Additionally, (C) illustrates the dependence of nucleation density on growth temperature. From [60]. Reprinted with permission from AAAS.

growth) are likely to dominate during the early stages of MOCVD unless graphene continuity can be preserved. Selecting N-polar templates offers a promising route to broaden the process window, but the number of demonstrations remains limited, and the corresponding growth protocols require further development.

5.2.2. Sapphire substrates

Native templates face graphene degradation and volatility in aggressive environments, so graphene-coated sapphire templates have become a promising solution to address challenges in III-nitride growth [27, 51, 169, 202, 209, 219, 221, 253–257]. Unlike GaN and AlN templates, sapphire offers greater chemical inertness and thermal stability [245], enabling better preservation of the graphene interlayer during epitaxy. Most demonstrations of graphene-assisted III-nitride growth on sapphire have been performed on c-plane Al_2O_3. Although systematic comparisons between c-plane and non- or semi-polar sapphire remain limited, substrate orientation should not be regarded as neutral. This is supported by demonstrations of graphene-assisted N-polar GaN growth on non-polar sapphire [164], as well as by recent studies on r- and m-plane sapphire showing that the resulting GaN orientation depends on the exposed sapphire plane, surface pretreatment, and whether growth proceeds through remote, QvdW, or thru-hole epitaxy [258, 259].

Comparison of nucleation on graphene-covered GaN and sapphire templates (both with wet-transferred graphene) indicates denser nucleation on sapphire compared to GaN at the same temperature, as shown in figure 16. This difference is attributed to the ionicity of the underlying substrate: the stronger potential ionic surface field of sapphire penetrates monolayer graphene more effectively than that of GaN, enhancing remote interaction and nucleation site formation [60]. Meanwhile, the decrease in nucleation density with increasing growth temperature is consistent with standard nucleation theory, in which the island density scales as $N \propto (F/D)^{\chi}$, where F is the adatom arrival flux and D is the diffusion coefficient. Since D increases with temperature, $D \sim D_0 \exp(-E_d/k_B T)$, higher temperatures increase Ga adatom mobility and diffusion length on graphene, thereby reducing the density of stable nuclei [260, 261]. Thus, the higher nucleation density on graphene/Al_2O_3 compared with graphene/GaN reflects the stronger substrate-induced electrostatic interaction, whereas the temperature-dependent decrease reflects enhanced adatom diffusion.

In one of the earliest demonstrations of single-step high-temperature (1040 °C) GaN MOCVD growth on graphene-coated sapphire, nucleation occurred preferentially at naturally formed multilayer graphene ridges, followed by lateral spreading across the graphene-coated surface until coalescence [262]. The authors reported that graphene layers (on the order of ∼0.6 nm) were sufficient to obtain continuous and comparatively flat GaN, while thicker graphene coatings progressively shifted the structure toward that of conventional two-step GaN-on-sapphire growth [262]. Furthermore, GaN device stacks, directly grown on functionalized graphene, have been reported with reduced biaxial stress and dislocation density relative to that grown on bare sapphire, while avoiding the classic low-temperature GaN buffer step [263].

AlN growth has also been successfully demonstrated on graphene/sapphire templates using single-step high-temperature (1200 °C) MOCVD without prior modification of the graphene [219]. As discussed in chapter 2, DFT calculations reveal stronger binding and lower migration energy for Al adatoms on graphene than for Ga adatoms, promoting nucleation and thin film formation. AlN islands

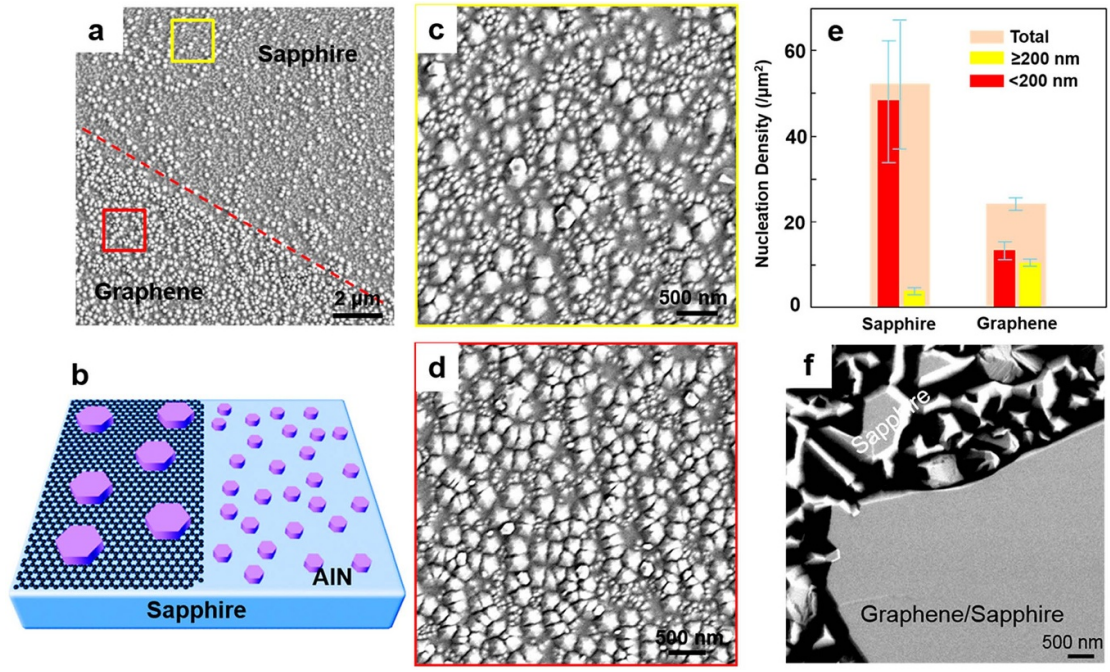

Figure 17. SEM analyses of AlN nucleation on bare sapphire and graphene-buffered sapphire. (a) A low-magnification SEM image with dense three-dimensional AlN nucleation on bare sapphire, in contrast to the lower nucleation density and more laterally extended island on graphene-coated sapphire. (b) A schematic representation of the distinct nucleation behaviors on the two substrates. (c) and (d) high-magnification SEM images showing the spatial distribution and morphology of AlN islands, demonstrating smaller, closely packed nuclei on bare sapphire (c) and larger, more isolated islands on the graphene-interfaced surface (d). (e) A quantitative statistical analysis of island density and lateral size for both cases. (f) An SEM image visualizes the evolution from non-coalescent to coalescent AlN domains. Reprinted with permission from [219]. Copyright (2018) American Chemical Society.

grown on graphene exhibit lower nucleation densities but larger lateral dimensions, indicating enhanced adatom surface diffusion. This behavior is consistent with nucleation theory: the dangling-bond-free graphene surface weakens adatom capture and lowers the effective migration barrier for Al-containing species, allowing them to diffuse over longer distances before incorporation. In contrast, a bare sapphire surface promotes dense, uniform, and smaller islands, typical of rapid nucleation and limited diffusion, as shown by SEM imaging (figure 17).

Additionally, single-step growth demonstrations emphasize defect-assisted chemical anchoring on graphene/sapphire, thereby increasing the density of stable nuclei and enabling rapid formation of smooth, single-crystalline AlN [38]. Beyond morphology, this high-density nucleation landscape alters the stress evolution during coalescence, partially compensating for compressive mismatch strain, and enabling low-residual-strain AlN films on sapphire [253].

Early studies primarily examined the physics of adsorption, the dependence of graphene thickness and substrate ionicity on epitaxial regimes, and largely overlooked the role of nanoscale defects. More recent work has expanded toward understanding how chemical doping and nanoscale defects in graphene influence epitaxy during MOCVD growth [81]. Three distinct growth modes on graphene-coated sapphire can arise depending on the nanoscale quality of the graphene layer: pristine, nitrogen-doped, and pinhole-formed. Correspondingly, three types of GaN microcrystallites emerged on the top, as shown in figure 18, each exhibiting different nucleation densities, strain states, and crystalline quality.

Pristine graphene enables the formation of well-aligned and strain-relaxed GaN crystallites (figure 19). This occurs because the undisturbed graphene transmits the periodic cation-anion surface potential of the Al_2O_3 substrate, allowing GaN to nucleate according to the template's charge pattern. In contrast, N-doped graphene compromises the fidelity of remote charge transfer. The doped sites act as chemically active anchoring points, increasing the nucleation density but also disrupting the remote epitaxial interactions. This produces a mixed growth regime; even so, the absence of direct GaN-Al_2O_3 bonding keeps the overall strain relatively low. Graphene-containing nanoscale pinholes lead to epitaxial lateral overgrowth (ELOG). Through these openings, GaN forms covalent bonds directly with the sapphire substrate, ensuring good epitaxial alignment but introducing a higher in-plane compressive strain owing to the lattice mismatch between GaN and Al_2O_3.

Previous examples have focused on the fundamentals; however, one of the main goals of this technology is to grow thin membranes. To enable

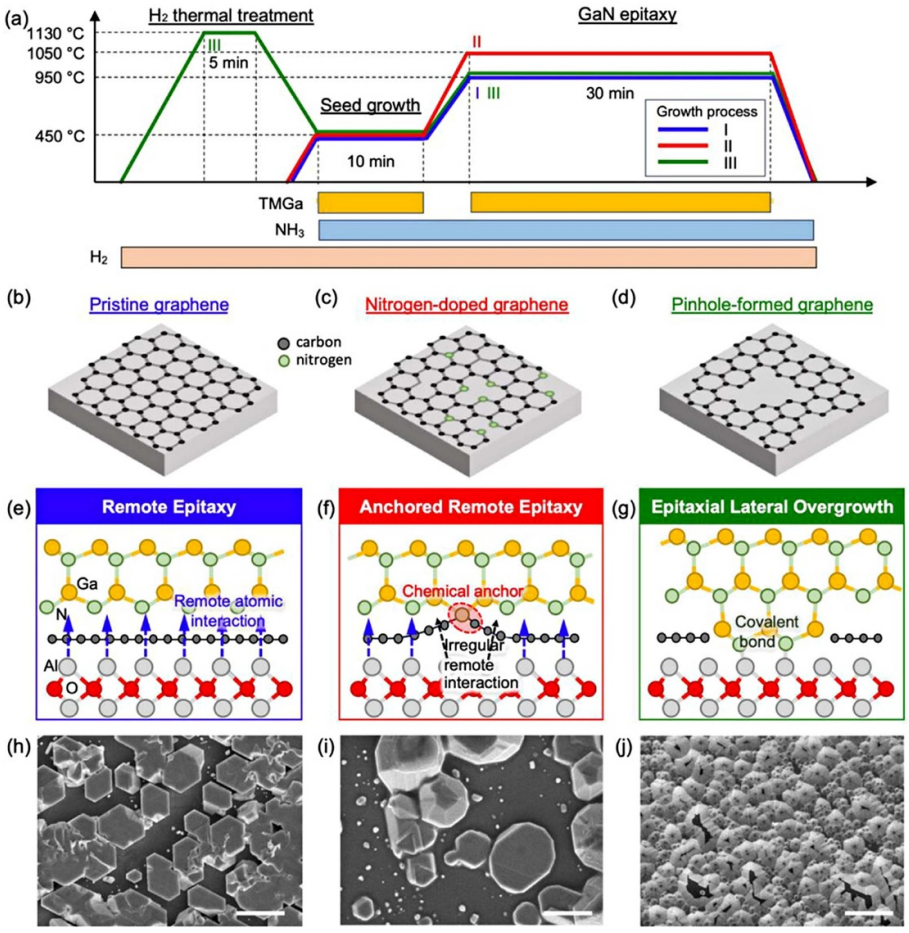

Figure 18. GaN growth on graphene-coated Al_2O_3. (a) MOCVD temperature and precursor/carrier-gas flow timing for three growth modes: remote epitaxy (process I, blue), anchored remote epitaxy (process II, red), and ELOG (process III, green). (b) and (d) Cartoon models of Al_2O_3 substrates covered by (b) pristine graphene, (c) N-doped graphene, and (d) graphene with nanoscale pinholes. (e)–(g) Corresponding cross-sectional sketches highlighting the interface structures and the dominant bonding/interaction pathways. (h)–(j) Top-view SEM micrographs of GaN crystallites formed on graphene/Al_2O_3 under remote epitaxy, anchored remote epitaxy, and ELOG conditions (left to right). Scale bars: 5 μm. [81] John Wiley & Sons. © 2025 The Author(s). Small published by Wiley-VCH GmbH.

the controlled lift-off of a high-quality GaN epilayer, a nearly single-crystalline bilayer graphene was grown directly on sapphire [169]. After in situ pretreatment in the MOCVD chamber, a ∼50 nm AlN nucleation layer was deposited in a high-temperature regime, followed by GaN growth using a 3D-to-2D growth sequence [169]. This approach leverages two complementary effects: nucleation is initiated at graphene defects, while enhanced adatom migration across intact graphene regions promotes lateral overgrowth and the development of a unified in-plane orientation. The resulting GaN exhibited low dislocation signatures, with XRD rocking-curve FWHM values of 0.22° for (002) and (0.32)° for (102) [169]. Importantly, the bilayer graphene interface mitigates the typical trade-off between epitaxial coupling and release: localized bonding at defect sites supports nucleation and alignment, whereas the largely vdW-coupled bilayer interface enables clean, controllable exfoliation of the GaN membrane from sapphire [169].

Functionalized graphene offers benefits when remote interaction is not feasible, but excessive modification can compromise exfoliation [27]. To preserve the pre-treated graphene and enhance lateral growth at elevated temperatures, pulsed-driven MOCVD was employed to modulate the precursor's interaction with graphene [209]. Therefore, a three-step growth procedure was selected: a low-temperature stage to achieve a high nucleation density, a pulse-driven intermediate-temperature stage to accelerate lateral coalescence, and a final high-temperature stage to improve crystallinity and yield a high-quality thin film. On/off-pulsed NH_3 flow at 1050 °C suppressed vertical overgrowth and preserved graphene. Scanning TEM (STEM) imaging confirmed the lateral GaN growth and bilayer graphene continuity (figure 20). In contrast, maintaining a continuous NH_3 flow suppresses lateral growth and increases the likelihood of graphene degradation.

Taken together, these studies show that nucleation on graphene-covered sapphire is strongly governed by

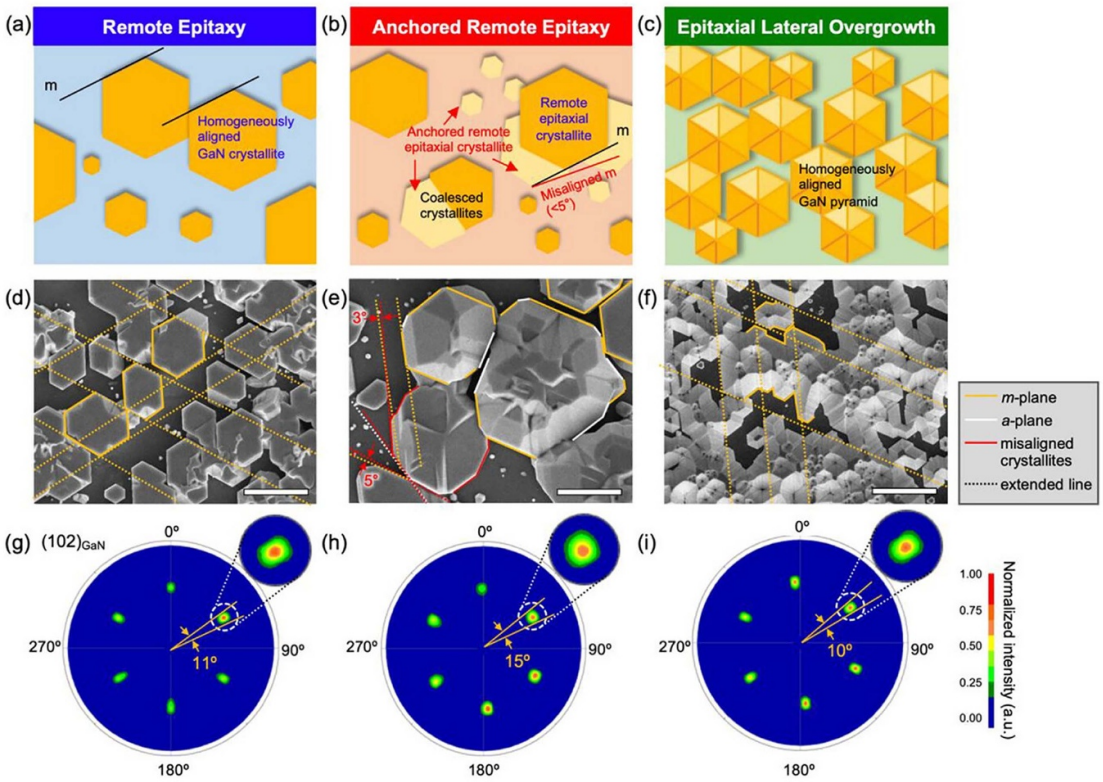

Figure 19. In-plane epitaxial alignment. (a)–(c) Plan-view schematics, (d)–(f) corresponding top-view SEM micrographs, and (g)–(i) XRD pole figures for GaN crystallites formed by remote epitaxy (a), (d) and (g), anchored remote epitaxy (b), (e) and (h), and ELOG (c), (f) and (i). Pole figures were collected from the GaN (102); zoomed views of the pole peaks are provided in the insets of (g)–(i). SEM scale bars: 5 μm. Peak widths in (g)–(i) were extracted using the null-to-null criterion. [81] John Wiley & Sons. © 2025 The Author(s). Small published by Wiley-VCH GmbH.

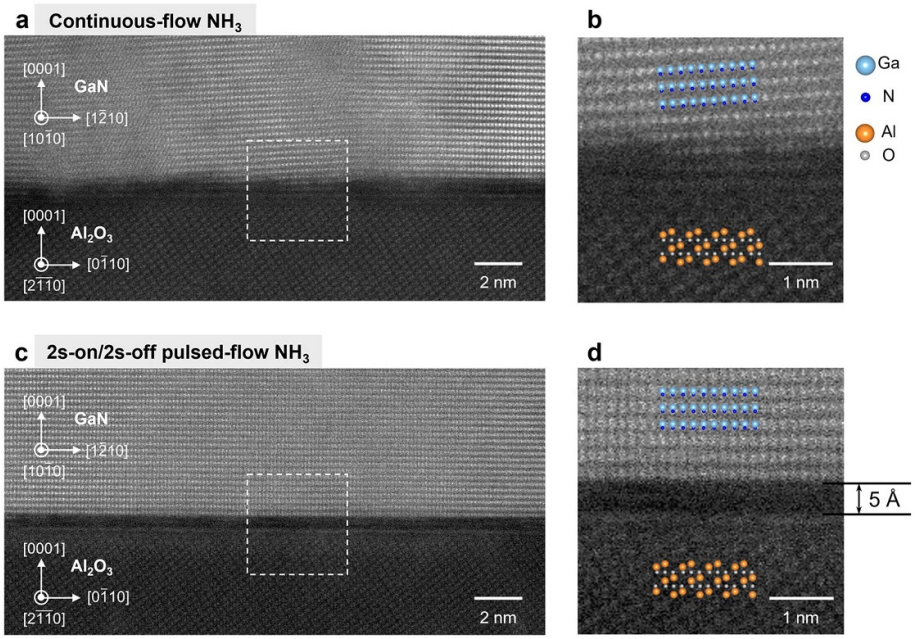

Figure 20. Cross-sectional STEM comparison of GaN grown on graphene-covered sapphire using (a) continuous and (b) pulsed NH_3 flow. Pulsed flow facilitates lateral overgrowth and preserves the graphene interlayer. Reprinted with permission from [209]. Copyright (2023) American Chemical Society.

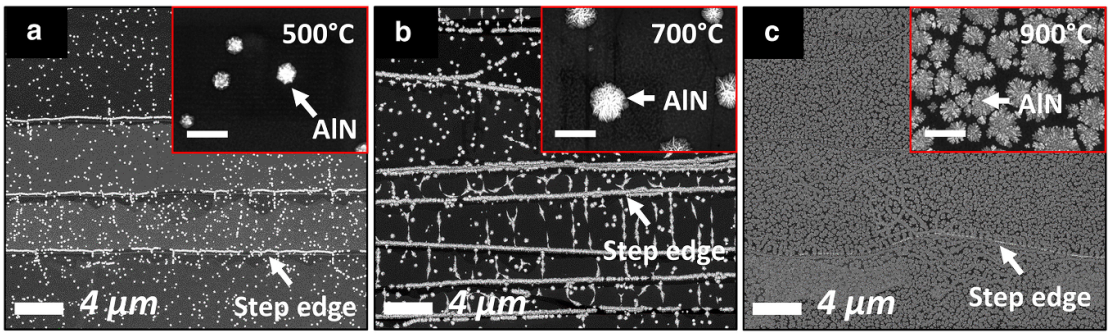

Figure 21. SEM images showing AlN nucleation on EG at (a) 500 °C, (b) 700 °C and (c) 900 °C. The inset scale bar corresponds to 400 nm. Reprinted from [220], Copyright (2015), with permission from Elsevier.

interfacial defects, whether deliberately engineered or introduced inadvertently. Because sapphire is chemically and thermally more robust than III-nitride templates, it supports a broader range of growth protocols and process windows. Even so, many successful demonstrations still depend on creating nucleation sites by locally disrupting or functionalizing graphene, indicating that strictly remote epitaxy is difficult to achieve under typical MOCVD conditions. In practice, QvdW growth has often emerged as a more reliable route to high-quality, exfoliable III-nitride films.

5.2.3. SiC substrates

The graphene/SiC platform is widely used as a testbed for graphene-assisted MOCVD of III-nitrides because it combines high thermal stability with an epitaxially compatible interface [216]. The transmission of SiC polarity and atomic registry through graphene is now well understood both computationally [62, 63] and experimentally [60, 201, 216, 231, 264, 265].

The nucleation of III-nitrides on EG-covered SiC occurs preferentially at step edges and defect sites [220]. The AlN series shown in figures 21(a)–(c) illustrates that two distinct mechanisms can govern the island density. Between 500 °C and 700 °C, the variation in AlN island size and density is consistent with the nucleation parameter F/D discussed above. At approximately fixed precursor supply, increasing temperature enhances the diffusion coefficient D, thus reducing the effective F/D ratio and increasing the adatom diffusion length. This promotes the formation of larger AlN islands and enhances adatom collection at step edges and pre-existing reactive sites on relatively intact EG.

However, the dense AlN nucleation observed at 900 °C in figure 21(c), should not be interpreted as a simple continuation of this diffusion-controlled trend. XPS analysis in [220] indicates the formation of C–N bonds following the 900 °C AlN nucleation step, and the marked increase in terrace nucleation density is attributed to nitrogen-related defects incorporated into the graphene lattice due to more efficient NH_3 decomposition at high temperatures. These defects increase the density of chemically active nucleation sites and can dominate over the decrease in F/D expected from enhanced surface diffusivity.

Highly aligned nucleation has been reported when the EG surface is pre-treated prior to growth [231]. In particular, annealing under H_2 and H_2/NH_3 atmospheres at approximately 1070 °C was used to tune the EG/SiC surface state. Notably, aligned GaN nucleation was observed only after the H_2/NH_3 pre-treatment. High-angle annular dark-field STEM indicated that the resulting seed islands exhibited an in-plane registry with the SiC(0001) lattice, while cross-sectional imaging showed a preserved graphene interlayer without evidence of direct thru-hole bonding at the interface (figure 22).

On graphitized SiC templates, GaN coalescence is typically achieved using growth sequences analogous to those on sapphire, including both single-step high-temperature growth and two-step protocols that separate nucleation and coalescence.

Recent work indicates that single-step high-temperature GaN overgrowth is successful when the graphene interlayer is directly synthesized on the substrate, with high thickness uniformity. For graphene/SiC, wafer-scale metal-assisted graphitization has been reported to suppress step bunching and multilayer graphene stripes commonly produced by conventional high-temperature SiC graphitization, yielding a more uniform graphene/SiC template for III-nitride overgrowth and membrane release [266]. In this approach, an AlN buffer was first deposited at 1050°C, followed by a single-step GaN growth at 1100°C [266]. These results define a practical boundary condition for single-step coalescence: when graphene remains continuous and local chemical anchoring is suppressed, high-temperature lateral overgrowth can occur while retaining a releasable interface.

In addition, a two-step MOCVD growth strategy can be employed to obtain smooth GaN on bilayer graphene/SiC [264]. This case represents a mixed

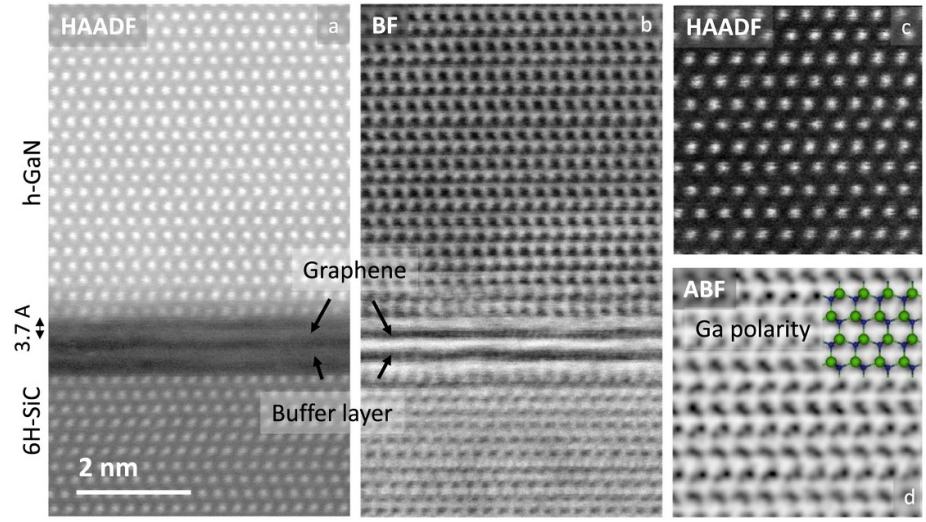

Figure 22. Dark- and bright-field cross-sectional TEM images of GaN nucleated on EG/SiC, showing preservation of the graphene interlayer and absence of direct bonding, consistent with remote epitaxy. Reproduced from [231]. © IOP Publishing Ltd All rights reserved.

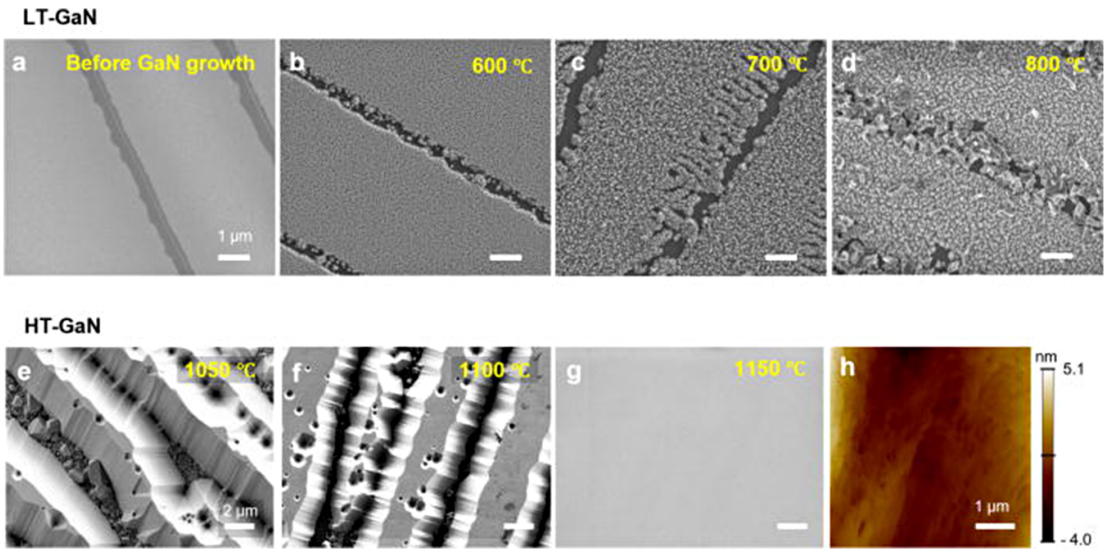

Figure 23. GaN layers were deposited on SiC with a graphene buffer layer template using MOCVD. (a) SEM image of the as-prepared graphene buffer layer surface prior to GaN growth. SEM micrographs of low-temperature GaN buffer layers formed at (b) 600 °C, (c) 700 °C, and (d) 800 °C (scale bars: 1 μm). SEM images of high-temperature GaN layers subsequently grown on 700 °C LT-GaN buffers at (e) 1050 °C, (f) 1100 °C, and (g) 1150 °C (scale bars: 2 μm). (h) AFM topography (5 μm$\pm$ 5 μm) corresponding to the HT-GaN surface obtained at 1150 °C in (g). Reprinted from [264], with the permission of AIP Publishing.

growth mode, in which the initial nucleation can be governed by remote interaction through graphene, defect- or step-assisted nucleation, graphene-thickness-dependent screening, and temperature-dependent adatom mobility. The process started with a low-temperature buffer layer deposited at 600 °C–800 °C for 5 min (figures 23(b)–(d)). At 600 °C temperature, dense columnar grains formed mainly on the graphene terraces, with minimal nucleation at the step edges, likely due to the attenuated substrate field in the bilayer regions. Raising the temperature to 700 °C improved the grain alignment and size, balancing adatom mobility and nucleation density. At a temperature of 800 °C, the excessive adatom mobility led to randomly oriented grains, thereby reducing layer crystallinity. Optimal nucleation conditions were identified at 700 °C, and subsequent high-temperature GaN growth at 1050, 1100, and 1150 °C further enhanced lateral coalescence (figures 23(e)–(g)).

Nevertheless, controlling nucleation and achieving full coalescence into continuous films remain challenging in pristine (untreated) EG/SiC systems. The electrostatic potential fluctuation across the untreated EG/SiC system was too weak to control the crystalline orientation [62]. Alternatively, systems

with a graphene buffer layer/single-layer graphene can be used for remote epitaxy on SiC. Experiments at 1050 °C showed a sharp decline in GaN nucleation density with increasing graphene thickness: from 3.8 ± 10^9 cm^{-2} on monolayer graphene to 1.5 ± 10^8 cm^{-2} on trilayer graphene [60]. This trend is consistent with the electrostatic field screening. In practice, graphene's thickness non-uniformity across the template can lead to the coexistence of multiple 2D-assisted growth regimes on SiC.

Beyond coalescence control, interfacial atomic engineering has been used to tune the epitaxial polarity of nitride layers on graphene/SiC templates [265]. In one approach, an NH_3 pretreatment at 1100 °C is followed by a short TMAl preflow prior to AlN buffer deposition, promoting the formation of interfacial Al-N bonding motifs, described as involving sp^3-hybridized bonds, which stabilize N-polarity through the AlN buffer and the subsequent GaN epilayer

Overall, these results suggest that graphene/SiC is a strong alternative to the native nitride and sapphire templates for graphene-assisted III-nitride epitaxy. The electrostatic guidance of the EG/SiC system can be improved through suitable surface treatments. In principle, a uniform monolayer graphene on SiC, free of step bunching and multilayer stripes, offers the most favorable pathway toward remote-registry transfer without relying on deliberate graphene modification.

5.2.4. Amorphous templates

Graphene-assisted III-nitride epitaxy has also been extended from crystalline templates to amorphous substrates such as silica glass, using both MOCVD [56, 267–270] and MBE [271]. Because amorphous materials lack long-range periodicity, direct nitride growth on bare amorphous surfaces typically yields polycrystalline films [272]. In this context, graphene is introduced as an interlayer that can (i) provide a chemically tailorable surface for controlled nucleation via vdW or QvdW epitaxy and (ii) decouple the growing nitride from the amorphous substrate, enabling improved out-of-plane texture and, under optimized conditions, enhanced in-plane ordering [56, 268].

One representative demonstration produced single-crystalline GaN on amorphous SiO_2/Si(100) using transferred monolayer graphene as an epitaxial buffer [268]. The graphene was pretreated in NH_3 at temperatures above 1100 °C, forming reactive C–N bonding configurations that promoted AlN nucleation primarily along graphene wrinkles. Interrupted-growth experiments revealed that subsequent GaN growth occurred preferentially on these AlN nuclei, forming GaN stripes that laterally expanded and coalesced into a continuous, smooth film (figure 24(a)). The resulting 2.5 μm-thick GaN layer exhibited atomic-step terraces and a step-flow surface morphology, with a reported RMS roughness of 0.46 nm [268].

Expanding on this concept, graphene was directly deposited onto amorphous SiO_2/Si without transfer, thereby avoiding contamination and mechanical deformation [56]. Nitrogen doping was induced via NH_3 exposure at 1100 °C, and AlN islands grown at 1200 °C on doped graphene exhibited high nucleation density and uniform hexagonal morphology (25–35 nm lateral size) compared to sparse, disordered nucleation on bare SiO_2 (figure 24(b)). These aligned AlN islands enable lateral GaN overgrowth, producing continuous films with improved in-plane ordering.

In addition to chemical functionalization, intermediate nanostructures have been used to amplify the crystallographic guidance on amorphous templates. For example, vertically oriented ZnO nanowalls on graphene/silica have been reported to act as alignment guides, promoting lateral overgrowth and a stronger *c*-axis texture, resulting in smoother GaN films [270]. A nanorod-assisted vdW epitaxy route was also demonstrated on graphene-coated silica glass, in which vertically aligned GaN nanorods nucleate at intentionally introduced graphene defect sites and serve as seeds for ELOG (figure 24(c)) [267]. XRD analysis indicated improved structural coherence, including reduced rocking-curve widths (FWHM $\sim 1.2°$) and lower dislocation densities compared with direct growth on amorphous substrates.

Overall, amorphous substrates highlight that the key requirement is not the underlying lattice periodicity, but the ability to engineer a dense, oriented nucleation template at the graphene surface. Consequently, controlling graphene modification (functional group chemistry, defect density, and thickness uniformity) remains central to improving the reproducibility, coalescence, and large-area film quality on graphene-coated amorphous supports. Thus, when no long-range substrate polarity is available, the reported cases are better described as graphene- or seed-assisted crystallographic alignment rather than direct substrate-imposed polarity transfer [56, 267, 268]. More generally, assigning a fixed epilayer polarity solely from the supporting substrate is difficult in graphene-assisted epitaxy. Even on crystalline templates, the final polarity and orientation can depend on the growth mode, graphene layer number and continuity, defect or pinhole density, surface pretreatment, and buffer/interface chemistry, as shown by polarity or orientation control on graphene/SiC and graphene/non-polar sapphire [39, 164, 167, 265].

6. Membrane exfoliation

Hybrid device architectures that combine free-standing semiconductor films with dissimilar host

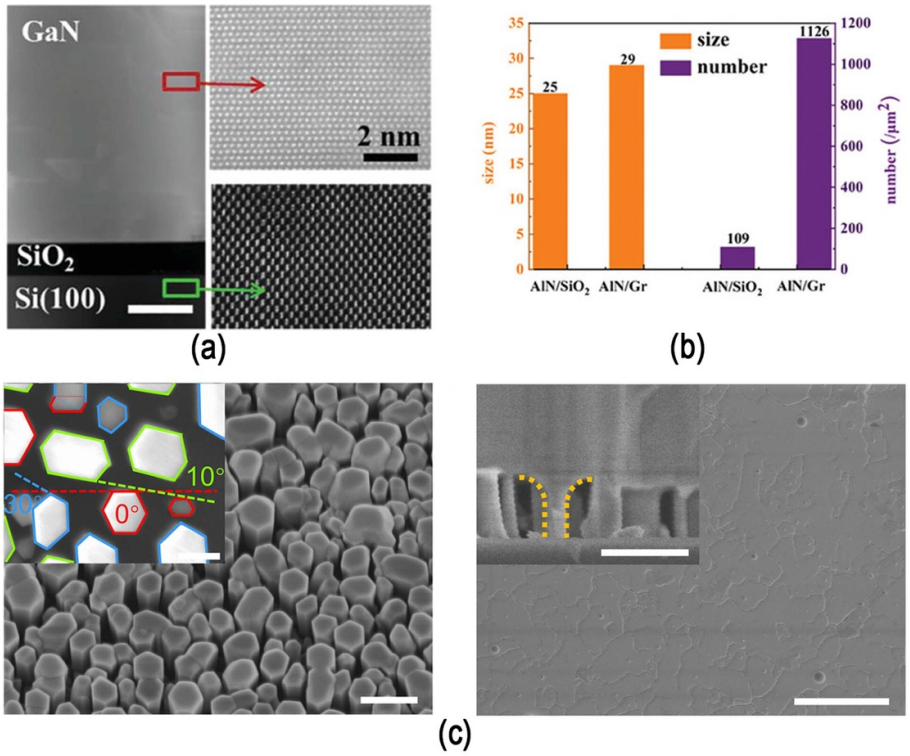

Figure 24. Graphene-assisted III-nitride epitaxy on amorphous templates. (a) Cross-sectional SEM image (left) and STEM images (right) of a 2.5 μm-thick GaN film grown on graphene-coated SiO_2/Si(100), showing the GaN/graphene/SiO_2 interface and crystalline ordering. [268] John Wiley & Sons. © 2019 WILEY-VCH Verlag GmbH & Co. KGaA, Weinheim. (b) SEM comparison of AlN nucleation on nitrogen-doped graphene/SiO_2/Si (left) versus bare SiO_2/Si (right), highlighting enhanced island density and symmetry on the modified graphene. [56] John Wiley & Sons. © 2024 The Authors. Advanced Science published by Wiley-VCH GmbH. (c) SEM image of GaN nanorods grown via nanorod-assisted vdW epitaxy on graphene/silica glass, showing vertically aligned, high-density growth suitable for coalescence. Scale bars, 5 μm (c right), 0.5 μm (c left, inset of c right), and 0.2 μm (inset of c left). From [267]. Reprinted with permission from AAAS.

platforms enable the development of multifunctional electronic and optoelectronic systems. By transferring epitaxial thin films onto thermally or structurally incompatible substrates, these approaches bypass conventional epitaxy constraints associated with lattice mismatch and limited thermal compatibility [20, 273]. This paradigm shift allows high degrees of heterogeneous integration for on-chip optical interconnects, micro-LED displays, flexible sensors, and wearable optoelectronics [19, 274, 275].

Epitaxial lift-off is a promising route for thin-film attachment and detachment [13, 15, 276]. Separation techniques assisted by 2D materials, particularly graphene, have proven especially effective. Graphene-assisted methods enable mechanical control of exfoliation, producing smoothly separated interfaces and allowing the detachment of thin III–V films with mild mechanical stimuli. This enables precise control over the membrane thickness while revealing information about the interfacial bonding and growth regime [14].

Numerous studies report the successful fabrication and exfoliation of III-nitride nanostructures and membranes grown by MOCVD on graphene interlayers [27, 51, 56, 59, 60, 62, 169, 207, 209, 215, 224, 238, 240, 242, 244, 264, 266–268, 277–281]. However, exfoliation remains delicate under mixed growth modes because strong, localized chemical interactions can hinder release. Exfoliation pathways commonly fall into two categories: stressor-free release [27, 169, 209, 224, 267] and stressor-assisted release using release-assist layers, such as metal films for spalling [62, 207, 215, 238, 242, 264, 266, 282]. In addition, chemical etching can be used to enable lift-off [281, 283]. Interfacial adhesion is a key parameter: too little adhesion on pristine graphene can cause self-delamination during cooling [27, 224], while excessive adhesion from defects or direct bonding makes separation difficult without applied stress [62, 207, 238, 242, 264].

A practical approach combines adhesion tuning through controlled defect introduction while avoiding large-area covalent bonding [27, 169, 224, 278]. In other cases, adhesion control is insufficient, and a metal stressor is required to achieve reliable large-area exfoliation [62, 169, 207, 215, 238, 242, 264, 266, 282].

6.1. Exfoliation with stressor

Nickel is the primary stressor of choice because it provides high internal stress and serves as a robust handling layer [282, 284, 285]. The deposition method

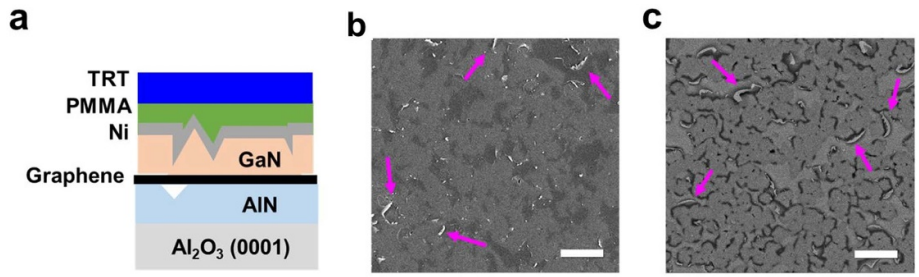

Figure 25. Exfoliation test on graphene/AlN with thin Ni/Ti stressor and PMMA planarization. (a) Schematic of the processed sample prepared for peel, (b) top-view SEM of GaN exfoliation from graphene/AlN, (c) top-view backscattered-electron SEM on the GaN/Ni/TRT stack after exfoliation. All scale bars are 5 μm; pink arrows mark nickel residue, consistent with incomplete load transfer when graphene-free pits act as anchors in the high-temperature case. Reprinted with permission from [207]. Copyright (2023) American Chemical Society.

and auxiliary metals determine the magnitude and uniformity of the driving forces. The main deposition approaches are direct sputtering or evaporation [62, 169, 207, 215, 242, 264, 286] and a two-step route that combines evaporation with electroplating [238, 282, 287, 288]. The latter is commonly employed in spalling-based release processes. In the electroplating route, a Ti/Au or Ti/Ni underlayer is first deposited, utilizing a thin Ti adhesion film to wet the III-nitride surface and bridge irregularities [288]. A thin Au or Ni capping layer prevents Ti oxidation while acting as a continuous seed for electroplating. Next, an electroplated Ni overlayer several microns thick is applied. The Ni layer stores sufficient elastic energy to facilitate debonding at the nitride/graphene interface [238]. Exfoliation can begin immediately after plating if the stress-thickness product exceeds the interfacial energy release rate. Although partial exfoliation can occur when graphene is damaged during high-temperature growth or when the electroplated Ni is nonuniform [238].

Fully sputtered or evaporated Ni stacks combined with a handling layer provide precise thickness control and generate a high residual stress, although typically at a lower throughput [169, 242]. A uniform thickness produces an even stress distribution. On GaN on graphene/AlN templates, an e-beam evaporated stack (Ni 300 nm/Ti 30 nm) plus a PMMA overcoat was used to planarize mesoscale roughness and distribute the peel load, which reduces stress concentrations and prevents premature failure of the metal-tape stack [207]. Despite these measures, film continuity often suffers from template pits or suboptimal growth, a contrast that is VIS between systems with uniform interfaces (figure 25), and systems that develop anchoring sites during high-temperature coalescence.

GaN grown on a graphene bilayer produced by the controlled graphitization of SiC shows narrow rocking curves and an atomically abrupt junction between GaN, graphene, and SiC (figure 26) [264]. Macroscopic demonstration of nickel stressor-assisted lift-off left terrace step signatures on exfoliated graphene/SiC. Electron backscatter diffraction (EBSD) confirmed the efficient coupling of tensile Ni and TRT to induce an interfacial crack without degrading the crystal quality. Complementary studies indicate that a sputtered Ni stressor on the GaN/graphene/sapphire surface develops a residual tensile stress near 660 MPa (figure 27) [169]. The strain-thickness relation identifies a critical thickness near 3 μm, yielding an interfacial toughness of roughly 2.3 J m^{-2}, which exceeds typical purely vdW values [289, 290] and indicates partial interfacial bonding formed during MOCVD, while retaining sufficient weakness for clean exfoliation. Raman mapping and surface imaging showed that the fracture occurred precisely along the bilayer graphene interface [169].

Taken together, these metrics indicate that graphene-enabled release follows a distinct mechanism compared to bulk GaN spalling, in which crack initiation and propagation must be carefully managed and generally require higher applied stress and a thicker stressor. Traditional spalling typically requires electroplated Ni with thicknesses on the order of 16 μm at 500 MPa or 8 μm at 800 MPa to achieve steady-state propagation, implying an effective fracture toughness of $\sim$ 1.7 MPa·m$^{1/2}$ for GaN [282]. In contrast, the graphene-assisted route works best with thinner or similarly/less-stressed Ni films, where cracks preferentially follow the weaker interface [169]. If the growth chemistry partially hybridizes the contact, the interface becomes significantly tougher. In this scenario, higher residual stress and finite critical thickness are required.

Overall, the design rule is to match the stressor's strain to the targeted release energy while preserving graphene integrity, ensuring that the intended interfacial crack path remains available. The relatively high residual stresses and finite critical stressor thicknesses suggest that high-temperature MOCVD can partially strengthen the interface, likely through local chemical bonding, so stronger stressors or modified

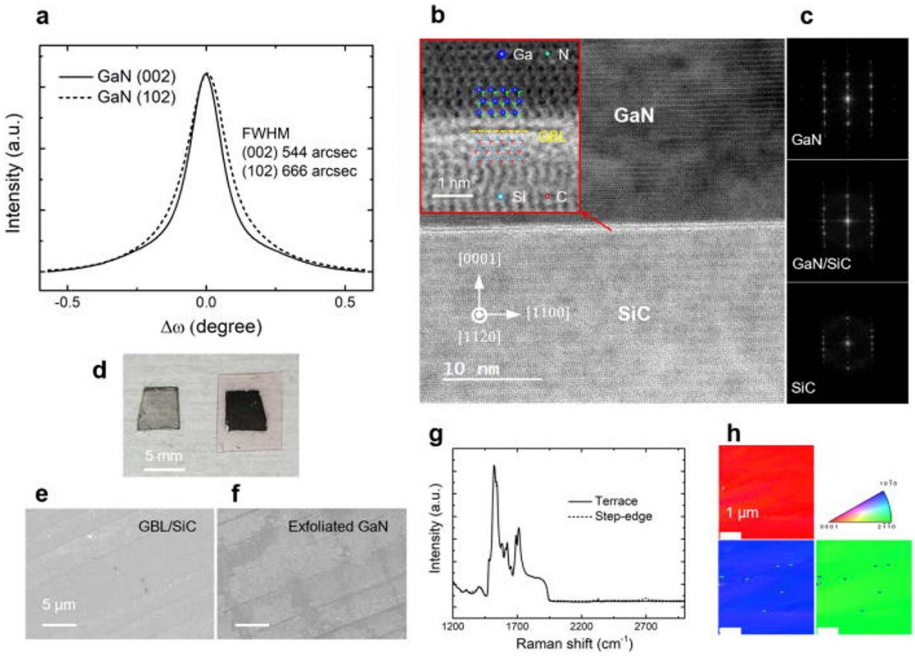

Figure 26. GaN on graphene buffer layer for Ni-stressor-assisted release. (a) x-ray rocking curves of GaN (002) and (102) exhibit full-widths at half-maximum near 544 and 666 arcsec, (b) cross-sectional annular bright-field TEM and (c) corresponding FFTs resolve the GaN/graphene buffer layer/SiC interface, (d) a photograph documents macroscopic lift-off of the GaN membrane onto TRT, (e) SEM views of the post-lift SiC template and (f) membrane bottom surface (5 μm scale bars), (g) Raman spectra on terraces and step edges, and (h) EBSD inverse-pole-figure maps (1 μm scale bar) collectively indicate a clean interfacial separation with preserved crystallinity. Reprinted from [264], with the permission of AIP Publishing.

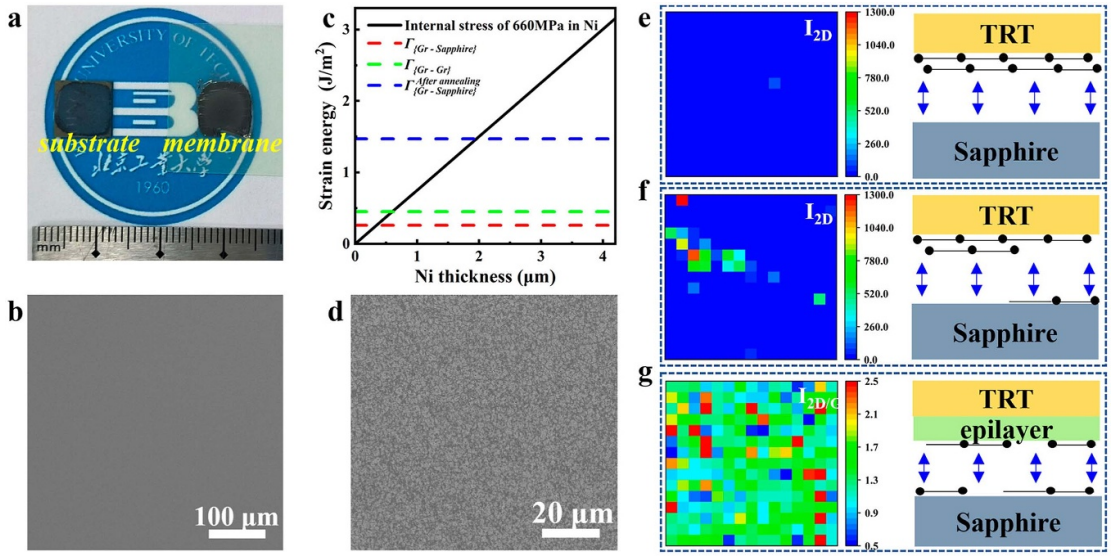

Figure 27. Ni-stressor-assisted lift-off of a GaN membrane grown on bilayer graphene/sapphire. (a) Photographs of the template and released membrane. SEM images of (b) the post-lift-off template surface and (d) the underside of the membrane. (c) calculated strain energy in the Ni stressor as a function of Ni thickness. (e)–(g) Raman maps indicating that fracture occurs at the bilayer-graphene interface. Reprinted with permission from [169]. Copyright (2025) American Chemical Society.

growth sequences may be required [169, 289, 290]. At the same time, residual stress is not only a mechanical release parameter: in wurtzite III-nitrides, strain modifies the band structure, near-band-edge emission, Raman phonon positions, and piezoelectric polarization fields that control quantum-confined Stark effects in LEDs and carrier confinement in HEMT structures [291–295]. Although exfoliation can partly relax heteroepitaxial mismatch stress, bending, attachment to a new support substrate, thermal-expansion mismatch, metal stressors, and locally pinned graphene defects can reintroduce nonuniform tensile or compressive strain; therefore, transferred membranes should be reevaluated.

6.2. Stressor-free

Maintaining an intact, inert 2D interlayer while preventing strong chemical anchoring keeps the vdW interface the weakest link, such that the modest, broadly distributed peel energy from TRT can sustain interfacial crack growth. In this metal-stressor-free regime, exfoliation depends on maintaining the interfacial toughness within a window set by the integrity and chemistry of the 2D layer, rather than on a large elastic-energy reservoir in an overlayer. The most effective demonstrations combine two features: resilient templates that withstand high temperatures and growth methods that minimize damage to graphene during nucleation and coalescence [60, 209, 240, 244, 267, 278, 296]. Process window studies clarify how easily weak interactions are lost on native substrates [240]. On graphene-coated sapphire, pulsing ammonia during MOCVD enables tape-only exfoliation [209], although a metal stressor is still used for the optimal yield, indicating an uneven adhesion landscape.

Patterning graphene to define sparse nucleation studs while retaining overall graphene continuity offers a complementary route to aid nucleation without sacrificing release [278]. Oxygen-assisted plasma can create localized small studs on an otherwise non-stick graphene background. During peeling, the crack percolates along the weakest continuous path, snapping the tiny studs by local fracture or debonding. Area-averaged adhesion remains sufficiently low for lift-off, and AlN, followed by GaN/LEDs grown on such templates, was transferred using commercial TRT. Raman mapping, diffraction, and device electroluminescence confirm that the vdW interface remains the preferred crack path [278].

Stressor-free peeling extends beyond the crystalline substrates. Using TRT on graphene-glass templates, GaN epilayers and LEDs were detached and transferred to flexible receivers [267]. In one protocol, a polymer gel was spin-coated and baked onto the GaN epilayer grown on a 2-inch graphene-glass wafer. The cured polymer and epitaxial layer were mechanically exfoliated using TRT. The absence of a metal stressor indicates that when the template does not provide pinning pathways through graphene imperfections, adhesive loads are sufficient for clean delamination, and post-transfer structural and optical metrics remain device-grade, even when the films are grown on an amorphous wafer.

Small-scale architectures further demonstrate tape-based release. Remote epitaxy has been used to grow GaN micro- and mesoscale structures on graphene, which were detached using adhesive tape and integrated into flexible white LEDs [296]. Although not continuous membranes, these results show that when the interface is unequivocally vdW and free of bonded anchors, modest adhesive energy can propagate cracks without a metal film.

Together, these studies define a narrow operating window for stressor-free exfoliation: preserving a large-area continuous interlayer, maintaining growth conditions that neither etch nor puncture the 2D layer, and avoiding roughness or pit-mediated pinning that would localize the peel front. When these criteria are met, TRT supplies sufficient and controllable mechanical input for clean delamination, with reported outcomes ranging from submicrometer to wafer-scale continuity, atomically abrupt interfaces, intact graphene 2D Raman bands, and functional post-exfoliation devices.

7. Future outlook

There are still challenges in achieving pure remote epitaxy of III-nitrides through MOCVD, particularly regarding the interface integrity and process windows. The degradation of interfacial graphene is influenced by various factors, including temperature, ambient conditions, defect density, and processing time. Frequently, the transfer step is the primary concern. While growing graphene directly on the substrate presents an alternative, it renders remote epitaxy highly dependent on the substrate, owing to unoptimized growth procedures on different materials.

From a practical outlook, the relevance of graphene-assisted III-nitride epitaxy is ultimately determined by the lateral scale over which both epitaxial growth and membrane release can be controlled. Wafer-scale epitaxy and wafer-scale exfoliation should therefore be treated as related but distinct benchmarks. The largest explicitly reported scales for the main graphene-based templates are summarized in table 3. These comparisons show that most platforms have reached wafer-scale template preparation or epitaxy in some form, but reproducible wafer-scale release remains the more restrictive benchmark.

Desired outcomes, such as stress reduction, integration on mismatched substrates, exfoliation, and substrate reuse can be accomplished through complementary vdW, QvdW, or thru-hole regimes, all of which can be enhanced by remote interactions. Recent studies have emphasized the interplay among these growth modes, utilizing quantitative criteria such as pinhole density, adhesion energy, and nucleation scaling. Nonetheless, there is a pressing need for a more systematic criterion to define each growth regime alongside the development of a unified theory for growth on the vdW surface.

Regardless of these challenges, research on remote epitaxy remains compelling because of the advantages of a remote registry without bonding, which enables the formation of clean, high-resilience membranes, alongside the benefits of 2D material epitaxy.

Table 3. Reported lateral scale and practical limitations for graphene-assisted III-nitride epitaxy and exfoliation on representative templates. The listed scale corresponds to the largest explicitly demonstrated graphene-assisted nitride growth or transfer area in the cited reports; when the substrate/template size and the active graphene area differ, this distinction is indicated.

Template	Largest demonstrated scale	Exfoliation feasibility	Main limitation	References
Graphene on III-nitrides	Mostly small-scale active graphene areas, typically around 1×1 cm^2. A 2 inch and 4 inch AlN/sapphire templates were used in a newer study.	Usually, small-scale exfoliation or stripping is demonstrated. Recent demonstrations report wafer-scale exfoliation.	Scaling is limited by the transferred graphene continuity and graphene damage during high-temperature nitride growth. GaN templates and H_2-rich or high-temperature conditions are especially challenging for release.	[207, 238, 240, 242, 244, 280]
Graphene/ sapphire	A 4 inch platform has been used for graphene-assisted epitaxy.	Wafer-level lift-off has been shown in optimized bi- and multi-layer graphene/sapphire systems. Monolayer graphene-coated sapphire has also enabled GaN epitaxy, although exfoliation is not always the primary target.	Often requires pretreatment. The main challenge is to balance epitaxial registry with sufficiently weak interfacial adhesion for controlled release.	[27, 169, 209, 224, 280]
Graphene/SiC	A 4 inch platform has been demonstrated for III-nitride graphene-assisted epitaxy.	III-nitride membrane exfoliation from graphene/SiC has been demonstrated. However, despite the 4 inch graphene/SiC platform, full-wafer III-nitride membrane release has not yet been clearly established; representative exfoliation demonstrations remain mainly at a small scale.	Wafer-scale uniform graphitization, control of graphene thickness and the GBL/SiC interface, step-bunching or multilayer graphene stripes, catalyst residues, and stress management during membrane release remain key constraints.	[62, 215, 264, 266, 277]
Graphene/glass	A 2 inch template has been used for graphene-assisted epitaxy.	Lift-off and transfer of flexible nitride LED structures from glass have been demonstrated.	The amorphous substrate requires special nucleation strategies, such as nanorod-assisted growth, and the material quality and device uniformity remain less mature than on crystalline templates.	[267]
Graphene on amorphous SiO_2/Si	A 4 inch platform has been used for graphene-assisted epitaxy.	Wafer-level peeling and crack-free transfer of III-nitride membranes have been reported in the newest Si-compatible Gr/SiO_2/Si(100) approach, although detailed materials/device demonstrations include smaller samples.	Thermal mismatch, crack-free wafer-scale peeling, uniformity of direct-grown graphene, nucleation control, and the graphene/SiO_2 interface remain key constraints. This route is promising for CMOS-compatible processing but remains an emerging approach.	[56, 268, 281]

Promising studies have been conducted on direct graphene growth to achieve the optimal conditions for remote epitaxy. Direct growth increases the substrate/process coupling. However, there is still a vast opportunity for the graphene community to explore novel template preparation methods. Additionally, systematic studies on various types of graphene, focusing on crystallinity, grain size, and conditioning before transfer or growth, are essential for improving the epitaxy procedure.

Research papers often select only one or two preparation methods for graphene, thereby increasing the risk of misclassifying the regime. Expanding methodologies can significantly influence the pace of graphene-assisted III-nitride growth. The industry may prefer to shift toward simpler methods for standard MOCVD 2D material growth, such as vdW, QvdW, or thru-hole epitaxy, instead of solely relying on remote epitaxy. However, nucleation on graphene and the transition between growth regimes are the least understood steps in these methods.

Additionally, exploring alternative 2D materials [31], such as amorphous carbon [163, 297], h-BN [298–300], transition-metal dichalcogenides [301, 302], and MXenes [303], could offer potential advantages for specific process windows. New graphene-assisted epitaxy concepts, including long-range remote epitaxy and hypotaxy, have recently been proposed and may help improve the crystalline registry under challenging growth conditions [304, 305]. Establishing standardized metrics such as adhesion, electrostatics, and nucleation scaling is crucial for achieving reliable and controllable nitride membrane technology.

The graphene-assisted strategy focuses on exfoliation of freestanding membranes and their subsequent heterogeneous integration. Current challenges in exfoliation include achieving an entirely uniform

release, managing post-exfoliation stress, controlling contamination, and facilitating substrate reuse. Recent research has emphasized that large-scale, continuous exfoliation without stress-inducing layers remains a challenge, underscoring the technological hurdles to achieving this goal.

If these challenges can be overcome, there is significant potential for the development of multilayered stacked membranes and hybrid electronics to complement or replace organics in niches that require high brightness and thermal stability [306]. Organic materials are susceptible to moisture and heat, and they have limitations related to the brightness and lifespan of blue light. In contrast, III-nitrides offer very high brightness, long lifetimes, and excellent stability in humid and high-temperature environments, along with rapid response times on a nanosecond scale [307]. Graphene-assisted techniques offer several advantages, including enhanced thermal management, improved packaging, increased interconnect reliability, greater resistance to bending fatigue, cost efficiency [12], and enhanced mass transfer [275].

For now, III-nitrides dominate the field of novel devices, particularly in the realm of light-emitting devices [308–311]. Progress has already been made in flexible and microLED technologies [308, 312–317], as well as in HEMTs [4, 5, 318]. However, a wide variety of UV, harsh-environment, piezoelectric, biointerface, flexible devices are yet to be realized, presenting a niche opportunity.

Novel device growth has already begun using graphene-covered templates, with LED fabrication being the dominant application [22, 209, 257, 267, 319–321]. Nevertheless, industrial-scale production of LEDs and the exfoliation process are still in the early stages. Furthermore, the heterogeneous integration of GaN-enabled devices with Si-based CMOS technology is promising for overcoming the limitations posed by Moore's Law [56]. Additionally, there is potential for graphene-assisted epitaxy in HEMTs [280]. We expect radar systems and power electronics designed for efficient chargers and data centers to be fabricated on 2D vdW surfaces.

In the near future, graphene-assisted epitaxy is expected to be used primarily for substrate reuse and membrane exfoliation. As we look ahead, the focus will continue to expand into specific device transfers to thin, flexible technologies, particularly in the already existing microLED field. We anticipate the emergence of transferable optoelectronic switches [322–324], memory devices [325], as well as integrable components for terahertz systems based on III-nitrides [326, 327].

In summary, since the initial report on graphene-assisted epitaxy, the field has made significant advancements driven by both academic research and its industrial applications. Although the area is still in development, it continues to generate interest owing to its potential benefits. Progress is being made as some groups work to optimize remote epitaxy, whereas others demonstrate that alternative methods can yield outstanding results beyond strict remote interactions. Practical applications in the field of III–V semiconductors are expected to grow through the development of controlled interface engineering and membrane technologies.

Acknowledgments

Research was funded by the Research Council of Lithuania under Grant Agreement No. S-CERN-24-4. A K acknowledges funding from the Research Council of Lithuania (LMTLT) under Project No. P-MIP-24-264. D A acknowledges the 'Universities Excellence Initiative' programme by the Ministry of Education, Science and Sports of the Republic of Lithuania (Project No. S-A-UEI-23-6).

Data availability statement

No new data were created or analysed in this study.

Conflict of interest statement

The authors have declared that no competing interests exist.

ORCID iDs

Dominykas Augulis 0000-0002-9472-2068
Juras Mickevivius 0000-0003-1623-4138

References

[1] Moustakas T D and Paiella R 2017 *Rep. Prog. Phys.* **80** 106501
[2] Chen F, Ji X and Lau S P 2020 *Mater. Sci. Eng.:* R **142** 100578
[3] Li J, Wang J, Yi X, Liu Z, Wei T, Yan J and Xue B 2020 *III-Nitrides Light Emitting Diodes: Technology and Applications* vol 306 (Springer)
[4] Du C, Ye R, Cai X, Duan X, Liu H, Zhang Y, Qiu G and Mi M 2023 *J. Semiconduct.* **44** 121801
[5] Udabe A, Baraia-Etxaburu I and Diez D G 2023 *IEEE Access* **11** 48628–50
[6] Emilio M D P 2024 *GaN and SiC Power Devices: From Fundamentals to Applied Design and Market Analysis* (Springer) (https://doi.org/10.1007/978-3-031-50654-3)
[7] Storm D F, Hardy M T, Katzer D S, Nepal N, Downey B P, Meyer D J, McConkie T O, Zhou L and Smith D 2016 *J. Cryst. Growth* **456** 121–32
[8] Kucharski R, Sochacki T, Lucznik B and Bockowski M 2020 *J. Appl. Phys.* **128** 050902
[9] Boćckowski M and Grzegory I 2022 *Acta Phys. Pol. A* **141** 167–74
[10] Liu L and Edgar J H 2002 *Mater. Sci. Eng.:* R **37** 61–127

[11] Li G, Wang W, Yang W, Lin Y, Wang H, Lin Z and Zhou S 2016 *Rep. Prog. Phys.* **79** 056501
[12] Bae S H, Kum H, Kong W, Kim Y, Choi C, Lee B, Lin P, Park Y and Kim J 2019 *Nat. Mater.* **18** 550–60
[13] Song W, Chen Q, Yang K, Liang M, Yi X, Wang J, Li J and Liu Z 2023 *Adv. Funct. Mater.* **33** 2209880
[14] Roh I, Goh S H, Meng Y, Kim J S, Han S, Xu Z, Lee H E, Kim Y and Bae S H 2023 *Nano Converg.* **10** 20
[15] Chen R, Song Y, He R, Wang J, Li J and Wei T 2024 *Prog. Quantum Electron.* **98** 100536
[16] Park M, Maekawa T, Hwang K, Cable J, Noriyuki W, Choi K, Noh Y K, Oh Y, Baek Y and Lee K 2024 *Nat. Rev. Electr. Eng.* **1** 680–9
[17] Park B I, Kim J, Lu K, Zhang X, Lee S, Suh J M, Kim D H, Kim H and Kim J 2024 *Nano Lett.* **24** 2939–52
[18] Kim S I, Moon J Y, Bae S, Xu Z, Meng Y, Park J W, Lee J H and Bae S H 2025 *Small Methods* **9** 2401551
[19] Choi S H, Kim Y, Jeon I and Kim H 2024 *Adv. Mater.* **37** 2411108
[20] Gong Z 2021 *Nanomaterials* **11** 842
[21] Chen F *et al* 2022 *Int. J. Extrem. Manuf.* **4** 042005
[22] Yu J, Wang L, Hao Z, Luo Y, Sun C, Wang J, Han Y, Xiong B and Li H 2020 *Adv. Mater.* **32** 1903407
[23] Liang D, Wei T, Wang J and Li J 2020 *Nano Energy* **69** 104463
[24] Chen Q, Yang K, Liang M, Kang J, Yi X, Wang J, Li J and Liu Z 2023 *Nano Converg.* **10** 39
[25] Wang X, Choi J, Yoo J and Hong Y J 2023 *Nano Converg.* **10** 40
[26] Ji J, Kwak H M, Yu J, Park S, Park J H, Kim H, Kim S, Kim S, Lee D S and Kum H S 2023 *Nano Converg.* **10** 19
[27] Chen Y, Shi Z, Zhang S, Yue Y, Zang H, Ben J, Jiang K, Jia Y, Sun X and Li D 2023 *ACS Appl. Mater. Interfaces* **15** 31954–65
[28] Kim H *et al* 2022 *Nat. Rev. Methods Primers* **2** 40
[29] Liu Z, Liu B, Chen Z, Yang S, Liu Z, Wei T, Gao P and Liu Z 2023 *Natl Sci. Open* **2** 20220068
[30] Xu Y, Wang J, Cao B and Xu K 2022 *Chin. Phys. B* **31** 117702
[31] Ryu H, Park H, Kim J H, Ren F, Kim J, Lee G H and Pearton S J 2022 *Appl. Phys. Rev.* **9** 031305
[32] Alaskar Y, Arafin S, Wickramaratne D, Zurbuchen M A, He L, McKay J, Lin Q, Goorsky M S, Lake R K and Wang K L 2014 *Adv. Funct. Mater.* **24** 6629–38
[33] Chan K T, Neaton J B and Cohen M L 2008 *Phys. Rev. B* **77** 235430
[34] Nakada K and Ishii A 2011 *Solid State Commun.* **151** 13–16
[35] Liu X, Wang C Z, Yao Y X, Lu W C, Hupalo M, Tringides M C and Ho K M 2011 *Phys. Rev. B* **83** 235411
[36] Liu X, Wang C Z, Hupalo M, Lu W C, Tringides M C, Yao Y X and Ho K M 2012 *Phys. Chem. Chem. Phys.* **14** 9157–66
[37] Rani B and Dharamvir K 2014 *Int. J. Quantum Chem.* **114** 1619–29
[38] Chen Z *et al* 2019 *Adv. Mater.* **31** 1807345
[39] Qu Y, Xu Y, Cao B, Wang Y, Wang J, Shi L and Xu K 2022 *ACS Appl. Mater. Interfacess* **14** 2263–74
[40] Hou R and Yang S 2023 *Chin. Phys. B* **32** 066801
[41] Malenfant-Thuot O, Moriniére M and Coté M 2024 *Nanotechnology* **35** 135702
[42] Wu H H, Li K, Song K, Zhang S M, Wang W H and Yang W 2025 *Surf. Interfaces* **56** 105560
[43] Talukder N, Wang Y, Nunna B B and Lee E S 2021 *Carbon* **185** 198–214
[44] Bhatt M D, Kim H and Kim G 2022 *RSC Adv.* **12** 21520–47
[45] Hong Y J and Fukui T 2011 *ACS Nano* **5** 7576–84
[46] Rasmussen J T, Gunst T, Bøggild P, Jauho A P and Brandbyge M 2013 *Beilstein J. Nanotechnol.* **4** 103–10
[47] Liu F *et al* 2022 *Adv. Mater.* **34** 2106814
[48] Nakada K, Ishii A and Yamamoto N 2013 *J. Korean Phys. Soc.* **63** 296–8
[49] Pašti I A, Jovanović A, Dobrota A S, Mentus S V, Johansson B and Skorodumova N V 2018 *Phys. Chem. Chem. Phys.* **20** 858–65
[50] Yan H, Ku P C, Gan Z Y, Liu S and Li P 2018 *Crystals* **8** 58
[51] Jia Y *et al* 2020 *Adv. Opt. Mater.* **8** 1901632
[52] Dai X, Shen T, Chen J and Liu H 2020 *Coatings* **10** 131
[53] Lehtinen P O, Foster A S, Ma Y, Krasheninnikov A and Nieminen R M 2004 *Phys. Rev. Lett.* **93** 187202
[54] Zhou Q, Ju W, Su X, Yong Y and Li X 2017 *J. Phys. Chem. Solids* **109** 40–45
[55] Wang X, Sun G, Routh P, Kim D H, Huang W and Chen P 2014 *Chem. Soc. Rev.* **43** 7067–98
[56] Liang D *et al* 2024 *Adv. Sci.* **11** 2305576
[57] Granzier-Nakajima T, Fujisawa K, Anil V, Terrones M and Yeh Y T 2019 *Nanomaterials* **9** 425
[58] Kong W *et al* 2018 *Nat. Mater.* **17** 999–1004
[59] Kim Y *et al* 2017 *Nature* **544** 340–3
[60] Chang C S *et al* 2023 *Sci. Adv.* **9** eadj5379
[61] Kim H *et al* 2021 *ACS Nano* **15** 10587–96
[62] Qiao K *et al* 2021 *Nano Lett.* **21** 4013–20
[63] Wang Y *et al* 2023 *ACS Nano* **17** 4023–33
[64] Liu F *et al* 2023 *Sci. Adv.* **9** eadf8484
[65] Jeong J, Min K A, Shin D H, Yang W S, Yoo J, Lee S W, Hong S and Hong Y J 2018 *Nanoscale* **10** 22970–80
[66] Chen Y, Gong X L and Gai J G 2016 *Adv. Sci.* **3** 1500343
[67] Yazdi G R, Iakimov T and Yakimova R 2016 *Crystals* **6** 53
[68] Mishra N, Boeckl J, Motta N and Iacopi F 2016 *Phys. Status Solidi (a)* **213** 2277–89
[69] Ullah S, Yang X, Ta H Q, Hasan M, Bachmatiuk A, Tokarska K, Trzebicka B, Fu L and Rummeli M H 2021 *Nano Res.* **14** 3756–72
[70] Sun B *et al* 2021 *Adv. Mater. Technol.* **6** 2000744
[71] Langston X and Whitener K E 2021 *Nanomaterials* **11** 2837
[72] Shan J, Sun J and Liu Z 2021 *ChemNanoMat* **7** 515–25
[73] Li Y, Zhou K, Ci H and Sun J 2023 *ChemSusChem* **16** e202300865
[74] Torres Quiñones J and Yun M 2023 *Microelectron. Eng.* **269** 111915
[75] Yang D, Ma F, Bian X, Xia Q, Xu K and Hu T 2024 *J. Phys.: Condens. Matter* **36** 173003
[76] Yin W, Liu C and Li J 2025 *Energy Environ. Mater.* **8** e70009
[77] Ma H, Chen X, Han Y, Zhang J, Wen K, Cheng S, Zhao Q, Wang Y, Wu J and Shao J 2024 *Adv. Sci.* **11** 2402319
[78] Zhang D, Yeo J Y, Zhang H, Yamaletdinov R, Yang Q, Zhan Y, Martin-Fernandez I, Yazyev O V, Toh C T and Özyilmaz B 2025 *Adv. Mater.* **37** e10545
[79] Zhao Y *et al* 2022 *Nat. Commun.* **13** 4409
[80] Nakatani M *et al* 2024 *Nat. Electron.* **7** 119–30
[81] Kim J *et al* 2025 *Small* **21** e03428
[82] Suk J W, Kitt A, Magnuson C W, Hao Y, Ahmed S, An J, Swan A K, Goldberg B B and Ruoff R S 2011 *ACS Nano* **5** 6916–24
[83] Pirkle A, Chan J, Venugopal A, Hinojos D, Magnuson C W, McDonnell S, Colombo L, Vogel E M, Ruoff R S and Wallace R M 2011 *Appl. Phys. Lett.* **99** 122108
[84] Lee W H *et al* 2012 *ACS Nano* **6** 1284–90
[85] Ambrosi A and Pumera M 2014 *Nanoscale* **6** 472–6
[86] Lupina G *et al* 2015 *ACS Nano* **9** 4776–85
[87] Wood J D *et al* 2015 *Nanotechnology* **26** 055302
[88] de Castro R K, Araujo J R, Valaski R, Costa L O O, Archanjo B S, Fragneaud B, Cremona M and Achete C A 2015 *Chem. Eng. J.* **273** 509–18
[89] Kim S, Shin S, Kim T, Du H, Song M, Lee C, Kim K, Cho S, Seo D H and Seo S 2016 *Carbon* **98** 352–7
[90] Zhang G, Güell A G, Kirkman P M, Lazenby R A, Miller T S and Unwin P R 2016 *ACS Appl. Mater. Interfaces* **8** 8008–16
[91] Chen M, Stekovic D, Li W, Arkook B, Haddon R C and Bekyarova E 2017 *Nanotechnology* **28** 255701
[92] Magnozzi M, Haghighian N, Miseikis V, Cavalleri O, Coletti C, Bisio F and Canepa M 2017 *Carbon* **118** 208–14

[93] Park H, Lim C, Lee C J, Kang J, Kim J, Choi M and Park H 2018 *Nanotechnology* **29** 415303
[94] De Fazio D *et al* 2019 *ACS Nano* **13** 8926–35
[95] Leong W S *et al* 2019 *Nat. Commun.* **10** 867
[96] Wu Z, Zhang X, Das A, Liu J, Zou Z, Zhang Z, Xia Y, Zhao P and Wang H 2019 *RSC Adv.* **9** 41447–52
[97] Qi P *et al* 2019 *Appl. Surf. Sci.* **493** 81–86
[98] Shahzad K, Jia K, Zhao C, Yan X, Yadong Z, Usman M and Luo J 2020 *Nanoscale Res. Lett.* **15** 85
[99] Kim H, Kim J C, Jeong Y, Yu J, Lu K, Lee D, Kim N, Jeong H Y, Kim J and Kim S 2021 *J. Appl. Phys.* **130** 174901
[100] Yoon M A, Kim C, Kim J H, Lee H J and Kim K S 2022 *Sensors* **22** 3944
[101] Jang D J, Haidari M M, Kim J H, Ko J Y, Yi Y and Choi J S 2023 *Nanomaterials* **13** 1494
[102] Caldwell J D *et al* 2010 *ACS Nano* **4** 1108–14
[103] Kim J, Park H, Hannon J B, Bedell S W, Fogel K, Sadana D K and Dimitrakopoulos C 2013 *Science* **342** 833–6
[104] Fechine G J M, Martin-Fernandez I, Yiapanis G, Bentini R, Kulkarni E S, Bof de Oliveira R V, Hu X, Yarovsky I, Castro Neto A H and Özyilmaz B 2015 *Carbon* **83** 224–31
[105] Bae S H *et al* 2017 *Proc. Natl Acad. Sci.* **114** 4082–6
[106] Luo D *et al* 2017 *Chem. Mater.* **29** 4546–56
[107] Kessler F, Muñoz P A R, Phelan C, Romani E C, Larrudé D R G, Freire F L, Thoroh de Souza E A, de Matos C J S and Fechine G J M 2018 *Appl. Surf. Sci.* **440** 55–60
[108] Kinoshita K, Moriya R, Onodera M, Wakafuji Y, Masubuchi S, Watanabe K, Taniguchi T and Machida T 2019 *npj 2D Mater. Appl.* **3** 1–8
[109] Yang S J, Choi S, Odongo Ngome F O, Kim K J, Choi S Y and Kim C J 2019 *Nano Lett.* **19** 3590–6
[110] Moon J Y, Kim S I, Son S K, Kang S G, Lim J Y, Lee D K, Ahn B, Whang D, Yu H K and Lee J H 2019 *Adv. Mater. Interfaces* **6** 1900084
[111] Shivayogimath A *et al* 2019 *Chem. Mater.* **31** 2328–36
[112] Kim J W, Woo J Y, Jo S, Oh J H, Hong W, Lee B C, Jung H J, Kim J H, Roh S C and Han C S 2020 *Appl. Surf. Sci.* **508** 145057
[113] Yílmaz K, Gürsoy M, Şakalak H, Ersöz M and Karaman M 2023 *ACS Appl. Eng. Mater.* **1** 2042–9
[114] Burton O J, Winter Z, Watanabe K, Taniguchi T, Beschoten B, Stampfer C and Hofmann S 2023 *ACS Nano* **17** 1229–38
[115] Bae S *et al* 2010 *Nat. Nanotechnol.* **5** 574–8
[116] Jang B, Kim C H, Choi S T, Kim K S, Kim K S, Lee H J, Cho S, Ahn J H and Kim J H 2017 *2D Mater.* **4** 024002
[117] Hempel M, Lu A Y, Hui F, Kpulun T, Lanza M, Harris G, Palacios T and Kong J 2018 *Nanoscale* **10** 5522–31
[118] Hong N, Kireev D, Zhao Q, Chen D, Akinwande D and Li W 2022 *Adv. Mater.* **34** 2106615
[119] Wang D Y *et al* 2013 *Adv. Mater.* **25** 4521–6
[120] Wang B, Huang M, Tao L, Lee S H, Jang A R, Li B W, Shin H S, Akinwande D and Ruoff R S 2016 *ACS Nano* **10** 1404–10
[121] Emtsev K, Speck F, Seyller T, Ley L and Riley J D 2008 *Phys. Rev. B* **77** 155303
[122] Poon S W, Chen W, Wee A T and Tok E S 2010 *Phys. Chem. Chem. Phys.* **12** 13522–33
[123] Luxmi S N, He G, Feenstra R and Fisher P 2010 *Phys. Rev. B* **82** 235406
[124] Pitsch S A and Sumathi R R 2023 *Crystals* **13** 189
[125] Emtsev K V *et al* 2009 *Nat. Mater.* **8** 203–7
[126] Zarotti F, Gupta B, Iacopi F, Sgarlata A, Tomellini M and Motta N 2016 *Carbon* **98** 307–12
[127] Hass J, Feng R, Li T, Li X, Zong Z, De Heer W, First P, Conrad E, Jeffrey C and Berger C 2006 *Appl. Phys. Lett.* **89** 143106
[128] De Heer W A, Berger C, Ruan M, Sprinkle M, Li X, Hu Y, Zhang B, Hankinson J and Conrad E 2011 *Proc. Natl Acad. Sci.* **108** 16900–5
[129] Kumar B *et al* 2016 *Physica E* **75** 7–14
[130] Zebardastan N, Bradford J, Lipton-Duffin J, MacLeod J, Ostrikov K, Tomellini M and Motta N 2023 *Nanotechnology* **34** 105601
[131] Zhu F *et al* 2024 *J. Cryst. Growth* **642** 127773
[132] Chatterjee A, Kruskopf M, Wundrack S, Hinze P, Pierz K, Stosch R and Scherer H 2022 *ACS Appl. Electron. Mater.* **4** 5317–25
[133] Han Y C, Yin S H, Zheng J R, Hu Y F, Sun L, Zhang L, Tian Z Q and Yi J 2024 *Adv. Funct. Mater.* **34** 2307298
[134] Fanton M A *et al* 2011 *ACS Nano* **5** 8062–9
[135] Michon A, Tiberj A, Vézian S, Roudon E, Lefebvre D, Portail M, Zielinski M, Chassagne T, Camassel J and Cordier Y 2014 *Appl. Phys. Lett.* **104** 071912
[136] Zhao Y *et al* 2014 *Chin. Phys. B* **23** 096802
[137] Wang G, Zhao Y, Deng Y, Huang W, Fan X, Zhang J, Duan R and Sun L 2015 *J. Phys. Chem. C* **119** 426–30
[138] Dagher R *et al* 2017 *Phys. Status Solidi a* **214** 1600436
[139] Ueda Y, Yamanda J, Fujiwara K, Yamamoto D, Maruyama T and Naritsuka S 2018 *Jpn. J. Appl. Phys.* **58** SAAE04
[140] Baek J, Kim J, Kim J, Shin B and Jeon S 2019 *Carbon* **143** 294–9
[141] Wei S, Ma L P, Chen M L, Liu Z, Ma W, Sun D M, Cheng H M and Ren W 2019 *Carbon* **148** 241–8
[142] Mischke J, Pennings J, Weisenseel E, Kerger P, Rohwerder M, Mertin W and Bacher G 2020 *2D Mater.* **7** 035019
[143] Yamada J, Ueda Y, Maruyama T and Naritsuka S 2020 *J. Cryst. Growth* **534** 125493
[144] Lou G, Ouyang Y, Xie Y, Wang W and Liu Z 2021 *Nanotechnology* **32** 475603
[145] Li J *et al* 2022 *Nat. Mater.* **21** 740–7
[146] Chang C J, Tsai P C, Su W Y, Huang C Y, Lee P T and Lin S Y 2022 *ACS Omega* **7** 13128–33
[147] Li M, Zou P, Chen Z, Zhao R, Tang C, Wang S, Ma Y and Ma L 2023 *ACS Appl. Nano Mater.* **6** 10817–25
[148] Ai D, Yu H, Ma Y, Cheng Y and Dong C 2024 *J. Cryst. Growth* **644** 127825
[149] Jankauskas Š, Meškinis Š, Žurauskienė N and Guobienė A 2024 *Nanomaterials* **14** 1635
[150] Akiyama K, Araki T, Murakami H, Kumagai Y and Koukitu A 2007 *Phys. Status Solidi c* **4** 2297–300
[151] Park J *et al* 2019 *Adv. Mater. Interfaces* **6** 1900821
[152] Oliveira M H, Schumann T, Gargallo-Caballero R, Fromm F, Seyller T, Ramsteiner M, Trampert A, Geelhaar L, Lopes J M J and Riechert H 2013 *Carbon* **56** 339–50
[153] Lopes J M J 2019 MBE growth of graphene *Molecular Beam Epitaxy: Materials and Applications for Electronics and Optoelectronics* eds H Asahi and Y Horikoshi (Wiley) pp 395–409 (available at: https://www.wiley.com/en-us/Molecular+Beam+Epitaxy%3A+Materials+and+Applications+for+Electronics+and+Optoelectronics-p-9781119355014)
[154] Lopes J M J and Vignaud D 2018 Molecular beam epitaxy of graphene and hexagonal boron nitride *Molecular Beam Epitaxy: From Research to Mass Production* 2nd edn (Elsevier) pp 487–513
[155] Wurstbauer U *et al* 2012 *Carbon* **50** 4822–9
[156] Hackley J, Ali D, DiPasquale J, Demaree J D and Richardson C J K 2009 *Appl. Phys. Lett.* **95** 133114
[157] Trung T T, Moreau E, Ferrer F J, Vignaud D, Wallart X and Godey S 2013 *Appl. Phys. Lett.* **102** 013118
[158] Trung T T, Moreau E, Ferrer F J, Vignaud D, Wallart X and Godey S 2014 *J. Appl. Phys.* **115** 223704
[159] Wang S, dos Santos L F, Wurstbauer U, Wang L, Pfeiffer L N, Hone J, Garcia J M and Pinczuk A 2014 *Solid State Commun.* **189** 15–20
[160] Albar J D, Summerfield A, Cheng T S, Davies A, Korolkov V V, Mellor C J, Khlobystov A N, Eaves L, Beton P H and Novikov S V 2017 *Sci. Rep.* **7** 6598
[161] Jerng S K, Lee J H, Yu D S, Kim Y S, Ryou J, Hong S, Kim C, Yoon S and Chun S H 2012 *Mater. Res. Bull.* **47** 2772–5
[162] Moreau E, Godey S, Ferrer F J, Vignaud D, Wallart X, Avila J, Asensio M C, Bournel F and Gallet J J 2010 *Appl. Phys. Lett.* **97** 241907
[163] Henksmeier T, Mahler P, Wolff A, Deutsch D, Voigt M, Ruhm L, Sanchez A M, As D J, Grundmeier G and Reuter D 2024 *Commun. Mater.* **5** 1–12

[164] Liu F et al 2020 Adv. Funct. Mater. 30 2001283
[165] Borisenko D P, Gusev A S, Kargin N I, Dobrokhotov P L, Timofeev A A, Labunov V A, Kovalchuk N G, Mikhalik M M and Komissarov I V 2021 J. Appl. Phys. 130 185304
[166] Song Y et al 2022 Adv. Mater. 34 2105851
[167] Park J H, Hu N, Park M D, Wang J, Yang X, Lee D S, Amano H and Pristovsek M 2023 Appl. Phys. Lett. 123 121601
[168] Littmann M, Reuter D and As D J 2023 Phys. Status Solidi b 260 2300034
[169] Feng Y et al 2025 ACS Appl. Electron. Mater. 7 2057–64
[170] Wang L, Lai R, Zhang L, Zeng M and Fu L 2022 ACS Mater. Lett. 4 528–40
[171] Terasawa T o and Saiki K 2015 Nat. Commun. 6 6834
[172] Wang Z J et al 2020 ACS Nano 14 1902–18
[173] Wang Z J et al 2015 ACS Nano 9 1506–19
[174] Liu Z, Lin Y C, Lu C C, Yeh C H, Chiu P W, Iijima S and Suenaga K 2014 Nat. Commun. 5 4055
[175] Patera L L et al 2013 ACS Nano 7 7901–12
[176] Puretzky A A, Geohegan D B, Pannala S, Rouleau C M, Regmi M, Thonnard N and Eres G 2013 Nanoscale 5 6507–17
[177] Jankowski M et al 2021 ACS Nano 15 9638–48
[178] Weatherup R S, Baehtz C, Dlubak B, Bayer B C, Kidambi P R, Blume R, Schlögl R and Hofmann S 2013 Nano Lett. 13 4624–31
[179] Gao L, Ren W, Li F and Cheng H M 2008 ACS Nano 2 1625–33
[180] Khadir S, Bon P, Vignaud D, Galopin E, McEvoy N, McCloskey D, Monneret S and Baffou G 2017 ACS Photonics 4 3130–9
[181] Masubuchi S and Machida T 2019 npj 2D Mater. Appl. 3 4
[182] Ivanov I G, Hassan J U, Iakimov T, Zakharov A A, Yakimova R and Janzén E 2014 Carbon 77 492–500
[183] Blake P, Hill E W, Castro Neto A H, Novoselov K S, Jiang D, Yang R, Booth T J and Geim A K 2007 Appl. Phys. Lett. 91 063124
[184] Yager T et al 2013 Nano Lett. 13 4217–23
[185] Panchal V et al 2018 Commun. Phys. 1 83
[186] Xiong F et al 2022 J. Mater. Chem. 10 6794–804
[187] Malard L M, Pimenta M A, Dresselhaus G and Dresselhaus M S 2009 Phys. Rep. 473 51–87
[188] Ferrari A C and Basko D M 2013 Nat. Nanotechnol. 8 235–46
[189] Wu J B, Lin M L, Cong X, Liu H N and Tan P H 2018 Chem. Soc. Rev. 47 1822–73
[190] Ferrari A C et al 2006 Phys. Rev. Lett. 97 187401
[191] Lee D S, Riedl C, Krauss B, von Klitzing K, Starke U and Smet J H 2008 Nano Lett. 8 4320–5
[192] Davydov V Y, Kitaev Y E, Goncharuk I, Smirnov A, Graul J, Semchinova O, Uffmann D, Smirnov M, Mirgorodsky A and Evarestov R 1998 Phys. Rev. B 58 12899
[193] Wang J, Zheng C, Ning J, Zhang L, Li W, Ni Z, Chen Y, Wang J and Xu S 2015 Sci. Rep. 5 7687
[194] Porto S P S and Krishnan R S 1967 J. Chem. Phys. 47 1009–12
[195] Calizo I, Bao W, Miao F, Lau C N and Balandin A A 2007 Appl. Phys. Lett. 91 201904
[196] Lee J E, Ahn G, Shim J, Lee Y S and Ryu S 2012 Nat. Commun. 3 1024
[197] Koo E and Ju S Y 2015 Carbon 86 318–24
[198] Huang L, Zhang D, Zhang F H, Feng Z H, Huang Y D and Gan Y 2018 Small 14 1704190
[199] Fan X, Wagner S, Schädlich P, Speck F, Kataria S, Haraldsson T, Seyller T, Lemme M C and Niklaus F 2018 Sci. Adv. 4 eaar5170
[200] Karmakar A, Vandrevala F, Gollier F, Philip M A, Shahi S and Einarsson E 2018 RSC Adv. 8 1725–9
[201] Yu Y et al 2021 Light Sci. Appl. 10 117
[202] Chang H et al 2020 Adv. Sci. 7 2001272
[203] Nemes-Incze P, Osváth Z, Kamarás K and Biró L P 2008 Carbon 46 1435–42
[204] Jiang T and Zhu Y 2015 Nanoscale 7 10760–6
[205] Lee H and Park J Y 2019 Rev. Sci. Instrum. 90 103702
[206] Chou H, Ismach A, Ghosh R, Ruoff R S and Dolocan A 2015 Nat. Commun. 6 7482
[207] Kwak H M et al 2023 ACS Nano 17 11739–48
[208] Choi J et al 2023 ACS Nano 17 21678–89
[209] Lee S et al 2023 Nano Lett. 23 11578–85
[210] Gao X, Li S, Bi J, Zhou K, Li M, Liu Z and Sun J 2024 Sci. China Chem. 67 824–40
[211] Kuech T F 2011 Integration of dissimilar materials Comprehensive Semiconductor Science and Technology vol 4 P Bhattacharya, eds R Fornari and H Kamimura (Elsevier) pp 1–24
[212] Ambacher O 1998 J. Phys. D: Appl. Phys. 31 2653
[213] Nakamura S et al 1991 Jpn. J. Appl. Phys. 30 L1705–7
[214] Li T et al 2018 Nanoscale Res. Lett. 13 130
[215] Kim J, Bayram C, Park H, Cheng C W, Dimitrakopoulos C, Ott J A, Reuter K B, Bedell S W and Sadana D K 2014 Nat. Commun. 5 4836
[216] Kakanakova-Georgieva A, Ivanov I G, Suwannaharn N, Hsu C W, Cora I, Pécz B, Giannazzo F, Sangiovanni D G and Gueorguiev G K 2021 CrystEngComm 23 385–90
[217] Journot T, Bouchiat V, Gayral B, Dijon J and Hyot B 2018 ACS Appl. Mater. Interfaces 10 18857–62
[218] Mun D H, Bae H, Bae S, Lee H, Ha J S and Lee S 2014 Phys. Status Solidi 8 341–4
[219] Qi Y et al 2018 J. Am. Chem. Soc. 140 11935–41
[220] Al Balushi Z Y, Miyagi T, Lin Y C, Wang K, Calderin L, Bhimanapati G, Redwing J M and Robinson J A 2015 Surf. Sci. 634 81–88
[221] Chen Y, Zang H, Jiang K, Ben J, Zhang S, Shi Z, Jia Y, Lü W, Sun X and Li D 2020 Appl. Phys. Lett. 117 051601
[222] Chung K, Lee C H and Yi G C 2010 Science 330 655–7
[223] Chang H et al 2019 Appl. Phys. Lett. 114 091107
[224] Guo Y et al 2025 Nano Energy 147 111614
[225] Ahmad W, Ullah Z, Sonil N I and Khan K 2021 J. Mater. Sci. Mater. Electron. 32 19991–20030
[226] Nepal N et al 2013 Appl. Phys. Express 6 061003
[227] Feng W, Long P, Feng Y and Li Y 2016 Adv. Sci. 3 1500413
[228] Felten A, McManus D, Rice C, Nittler L, Pireaux J J and Casiraghi C 2014 Appl. Phys. Lett. 105 183104
[229] Wang W, Zheng Y, Li X, Li Y, Zhao H, Huang L, Yang Z, Zhang X and Li G 2019 Adv. Mater. 31 1803448
[230] Whitener K E 2018 J. Vac. Sci. Technol. A 36 05G401
[231] Journot T, Okuno H, Mollard N, Michon A, Dagher R, Gergaud P, Dijon J, Kolobov A V and Hyot B 2019 Nanotechnology 30 505603
[232] Lee Y, Lee S, Choi J, Kim C and Kwon Y K 2024 Adv. Eng. Mater. 26 2301654
[233] Lee Y, Choi S H, Kim H and Yoo J 2025 Small Methods 9 2401815
[234] Li J, Xu Y, Tao J, Cai X, Wang Y, Wang G, Cao B and Xu K 2023 Cryst. Growth Des. 23 5541–7
[235] Barbier C et al 2023 Cryst. Growth Des. 23 6517–25
[236] Chen Q, Yin Y, Ren F, Liang M, Yi X and Liu Z 2020 Materials 13 3835
[237] Badokas K, Kadys A, Mickevičius J, Ignatjev I, Skapas M, Stanionytė S, Radiunas E, Juška G and Malinauskas T 2021 J. Phys. D: Appl. Phys. 54 205103
[238] Badokas K, Kadys A, Augulis D, Mickevičius J, Ignatjev I, Skapas M, Šebeka B, Juška G and Malinauskas T 2022 Nanomaterials 12 785
[239] Feng T, Zhang S, Yang K, Chen Q, Liang M, Yan J, Yi X, Wang J, Li J and Liu Z 2022 Adv. Opt. Mater. 10 2201262
[240] Han X et al 2022 ACS Appl. Electron. Mater. 4 5326–32
[241] Han X et al 2023 ACS Appl. Nano Mater. 6 15159–65
[242] Kwak H M et al 2023 ACS Appl. Mater. Interfaces 15 59025–36
[243] Yu J, Wang L, Han X, Hao Z, Luo Y, Sun C, Han Y, Xiong B, Wang J and Li H 2021 Opt. Mater. Express 11 4118–29
[244] Liu M, Zhou J, Lu Z, Wang Y, Wang L, Xu Y, Cao B, Wang J and Xu K 2025 Jpn. J. Appl. Phys. 64 031003
[245] Park J H, Yang X, Lee J Y, Park M D, Bae S Y, Pristovsek M, Amano H and Lee D S 2021 Chem. Sci. 12 7713–9

[246] Chang W, Popov B N and Li C 2021 *RSC Adv.* **11** 36354–9
[247] Mastro M, Kryliouk O, Reed M, Anderson T, Davydov A and Shapiro A 2001 *Phys. Status Solidi a* **188** 467–71
[248] Kumagai Y, Akiyama K, Togashi R, Murakami H, Takeuchi M, Kinoshita T, Takada K, Aoyagi Y and Koukitu A 2007 *J. Cryst. Growth* **305** 366–71
[249] Narayan J, Pant P, Chugh A, Choi H and Fan J C C 2006 *J. Appl. Phys.* **99** 054313
[250] Mohanty S, Khan K and Ahmadi E 2023 *Prog. Quantum Electron.* **87** 100450
[251] Li W *et al* 2023 *IEEE Trans. Electron Devices* **70** 2075–80
[252] Arias-Purdue A *et al* 2023 *IEEE Microw. Wirel. Technol. Lett.* **33** 1011–4
[253] Chang H *et al* 2022 *Light: Sci. Appl.* **11** 88
[254] Liu B *et al* 2022 *Nano Lett.* **22** 3364–71
[255] Kadys A, Mickevičius J, Badokas K, Strumskis S, Vanagas E, Podlipskas Ž, Ignatjev I and Malinauskas T 2023 *Nanomaterials* **13** 784
[256] Shi B *et al* 2024 *Nano Lett.* **24** 7458–66
[257] Fabunmi T G *et al* 2024 *Nanotechnology* **35** 085603
[258] Naritsuka S, Kato Y, Nonogaki M, Yokoi R, Osamura K, Yanase Y and Maruyama T 2024 *J. Cryst. Growth* **630** 127593
[259] An S Y *et al* 2026 *Cryst. Growth Des.* **26** 2713–23
[260] Ratsch C and Venables J A 2003 *J. Vac. Sci. Technol. A* **21** S96–S109
[261] Venables J A, Spiller G D T and Hanbucken M 1984 *Rep. Prog. Phys.* **47** 399–459
[262] Choi J K *et al* 2012 *Nanotechnology* **23** 435603
[263] Chen Z *et al* 2018 *Adv. Mater.* **30** 1801608
[264] Lee S *et al* 2024 *Appl. Phys. Lett.* **125** 252102
[265] Yu J *et al* 2024 *Appl. Surf. Sci.* **672** 160849
[266] Kim S H *et al* 2025 *Sci. Adv.* **11** eadz3605
[267] Ren F *et al* 2021 *Sci. Adv.* **7** eabf5011
[268] Feng Y *et al* 2019 *Adv. Funct. Mater.* **29** 1905056
[269] Ohta J, Shon J W, Ueno K, Kobayashi A and Fujioka H 2017 *IEICE Trans. Electron.* **100** 161–5
[270] Chung K, In Park S, Baek H, Chung J S and Yi G C 2012 *NPG Asia Mater.* **4** e24–e24
[271] Yu J, Hao Z, Deng J, Wang L, Luo Y, Wang J, Sun C, Han Y, Xiong B and Li H 2021 *Cryst. Growth Des.* **21** 3831–7
[272] Min J and Park K 2025 *Adv. Photon. Res.* **6** 2500014
[273] Kum H, Lee D, Kong W, Kim H, Park Y, Kim Y, Baek Y, Bae S H, Lee K and Kim J 2019 *Nat. Electron.* **2** 439–50
[274] Park M, Bae B, Kim T, Kum H S and Lee K 2022 *J. Appl. Phys.* **132** 190902
[275] Shin J *et al* 2023 *Nature* **614** 81–87
[276] Fu W Y and Choi H W 2022 *J. Appl. Phys.* **132** 060903
[277] Liu Y, Xu Y, Cao B, Li Z, Zhao E, Yang S, Wang C, Wang J and Xu K 2019 *Phys. Status Solidi a* **216** 1801027
[278] Jia Y *et al* 2021 *ACS Appl. Mater. Interfaces* **13** 32442–9
[279] Zhou H, Xu Y, Chen X, Liu Y, Cao B, Yin W J, Wang C and Xu K 2020 *J. Alloys Compd.* **844** 155870
[280] Wen Y *et al* 2025 *Adv. Mater.* **37** 2501916
[281] Gao Y *et al* 2025 *Adv. Sci.* **12** e12193
[282] Bedell S W, Lauro P, Ott J A, Fogel K and Sadana D K 2017 *J. Appl. Phys.* **122** 025103
[283] Gupta P, Rahman A, Hatui N, Parmar J B, Chalke B A, Bapat R D, Purandare S, Deshmukh M M and Bhattacharya A 2013 *Appl. Phys. Lett.* **103** 181108
[284] Bedell S W, Bayram C, Fogel K, Lauro P, Kiser J, Ott J, Zhu Y and Sadana D 2013 *Appl. Phys. Express* **6** 112301
[285] Park H *et al* 2022 *Sci. Adv.* **8** eabl6406
[286] Blanton E W, Motala M J, Prusnick T A, Hilton A, Brown J L, Bhattacharyya A, Krishnamoorthy S, Leedy K, Glavin N R and Snure M 2021 *Small* **17** 2102668
[287] Zhang H *et al* 2023 *Adv. Sci.* **10** 2205612
[288] Lee Y, Gupta B, Tan H H, Jagadish C, Oh J and Karuturi S 2022 *STAR Protoc.* **3** 101015
[289] Koenig S P, Boddeti N G, Dunn M L and Bunch J S 2011 *Nat. Nanotechnol.* **6** 543–6
[290] Wang W, Dai S, Li X, Yang J, Srolovitz D J and Zheng Q 2015 *Nat. Commun.* **6** 7853
[291] Kisielowski C *et al* 1996 *Phys. Rev. B* **54** 17745–53
[292] Yan Q, Rinke P, Janotti A, Scheffler M and Van de Walle C G 2014 *Phys. Rev. B* **90** 125118
[293] Bernardini F, Fiorentini V and Vanderbilt D 1997 *Phys. Rev. B* **56** R10024–7
[294] Ambacher O *et al* 1999 *J. Appl. Phys.* **85** 3222–33
[295] Waltereit P, Brandt O, Trampert A, Grahn H T, Menniger J, Ramsteiner M, Reiche M and Ploog K H 2000 *Nature* **406** 865–8
[296] Jeong J *et al* 2021 *Nano Energy* **86** 106075
[297] Voronenkov V V, Leonidov A A, Bochkareva N I, Gorbunov R I, Latyshev P E, Lelikov Y S, Kogotkov V S, Zubrilov A S and Shreter Y G 2019 *J. Phys.: Conf. Ser.* **1199** 012004
[298] Han M, Ryu B D, Ko K B and Hong C H 2023 *Phys. Status Solidi b* **260** 2200496
[299] Jiang M *et al* 2024 *Appl. Surf. Sci.* **659** 159902
[300] Yang P *et al* 2025 *ACS Appl. Electron. Mater.* **7** 9380–8
[301] Gupta P *et al* 2016 *Sci. Rep.* **6** 23708
[302] Chen Y, Shi Z, Zhang S, Ben J, Jiang K, Zang H, Jia Y, Lü W, Li D and Sun X 2022 *Adv. Electron. Mater.* **8** 2100759
[303] Yamunasree B, Thota C, Pandey A, Choppara S, Kshetri Y K, Kheawhom S, Murali G, Kim M D, In I and Reddeppa M 2025 *Laser Photonics Rev.* **19** e01261
[304] Moon D *et al* 2025 *Nature* **638** 957–64
[305] Jia R *et al* 2025 *Nature* **646** 584–91
[306] Kim T S, Ryu J E, Park J, Liu R J, Choi J, Kim J, Hong Y J, Kim D H and Shin J 2025 *Light Sci. Appl.* **14** 335
[307] Sugiura T 2025 *Electr. Mater. Appl.* **2** e70020
[308] Zhuang Z, Iida D and Ohkawa K 2021 *Jpn. J. Appl. Phys.* **61** SA0809
[309] Zhou S, Zhao X, Du P, Zhang Z, Liu X, Liu S and Guo L J 2022 *Nanoscale* **14** 4887–907
[310] Amir H A A A, Fakhri M A and Alwahib A A 2021 *Mater. Today* **42** 2815–21
[311] Buffolo M, Caria A, Piva F, Roccato N, Casu C, De Santi C, Trivellin N, Meneghesso G, Zanoni E and Meneghini M 2022 *Phys. Status Solidi a* **219** 2100727
[312] Bosch J, Durand C, Alloing B and Tchernycheva M 2024 *J. Inf. Disp.* **25** 61–73
[313] Lu T *et al* 2024 *Adv. Electron. Mater.* **10** 2400256
[314] Gu P, Yang S, Ma L, Yang T, Hou X, Mei Y, Ying L, Long H and Zhang B 2023 *Opt. Lett.* **48** 4117–20
[315] Yang S, Gu P, Yang T, Ma M, Ying L, Mei Y and Zhang B 2024 *ACS Photonics* **11** 1935–42
[316] Yue L *et al* 2024 *Jpn. J. Appl. Phys.* **63** 051007
[317] Wu H *et al* 2024 *Light Sci. Appl.* **13** 284
[318] Wu N, Xing Z, Li S, Luo L, Zeng F and Li G 2023 *Semicond. Sci. Technol.* **38** 063002
[319] Lee K, Yoo D, Oh H and Yi G C 2020 *Sci. Rep.* **10** 19677
[320] Singh A K, Ahn K, Yoo D, Lee S, Ali A, Yi G C and Chung K 2022 *NPG Asia Mater.* **14** 57
[321] Yoo D, Lee K, Tchoe Y, Guha P, Ali A, Saroj R K, Lee S, Islam A H, Kim M and Yi G C 2021 *Sci. Rep.* **11** 17524
[322] Fang S *et al* 2022 *Adv. Funct. Mater.* **32** 2202524
[323] Chen D *et al* 2023 *Nano Res.* **16** 5503–10
[324] Vashishtha P, Jain S K, Prajapat P, Verma A K, Aggarwal N, Murdoch B J, Walia S and Gupta G 2024 *ACS Appl. Opt. Mater.* **2** 1353–9
[325] Yu H, Liu H, Li L, Duan X, Peng Z, Lu L, Lin X and Chang K C 2025 *Adv. Funct. Mater.* **36** e13256
[326] Uzundal C B, Feng Q, Tang W, Hu C, Sanborn C, Yoon Y, Chen S, Ruan J, Louie S G and Wang F 2025 *Light Sci. Appl.* **14** 226
[327] Yu R, Liu D, Cai X, Zhou Q, Wang M, Jin L, Sun J, Li X and Qin H 2025 *Adv. Mater.* **37** 2507534